Investigation of the Finite Element Method for

Computing Wheel/Rail Contact Forces in Steady Curving

by

Eduardo Moas, Jr.

Thesis submitted to the Faculty of the

Virginia Polytechnic Institute and State University

in partial fulfillment of the requirements for the degree of

Master of Science

in

Mechanical Engineering

APPROVED:

Dr. Robert H. Fries, Chairman

Dr. Charles E. Knight

Dr. Robert G. Leonard

September, 1987

Blacksburg, Virginia

Investigation of the Finite Element Method for

Computing Wheel/Rail Contact Forces in Steady Curving

by

Eduardo Moas, Jr.

Dr. Robert H. Fries, Chairman

Mechanical Engineering

(ABSTRACT)

The understanding of rail vehicle steady-state and dynamic curving has increased substantially in the last few years. Contemporary curving models include such non-linear effects as two-point contact, creep force saturation, and rail flexibility. The usual approximation concerning the contact geometry is that the localized wheel and rail curvatures at the center of the contact patch are constant throughout the contact patch. This approximation allows computation of contact stresses using Hertzian theory, and it allows the computation of contact patch forces using one of Kalker's theories.

In vehicle curving, contact usually occurs at or near the wheel flange, where the wheel/rail contact geometry is non-Hertzian. Furthermore, after being in service for some time, the wheel and rail profiles provide non-Hertzian geometry due to wear. Both of these effects tend to invalidate the assumption of Hertzian contact geometry in the contact region.

This work uses a generic wheelset model which is the basic component of any rail vehicle model. The wheel/rail interaction is modelled using the finite element method. The wheel is generated as a surface of revolution of its tread profile, and the

rail is generated as an extrusion of the rail head profile. Three-dimensional contact elements are used to characterize the wheel/rail interface. A simple stick/slip friction model is used wherein relative motion is permitted if the tangential force exceeds the adhesion limit, and no relative motion occurs otherwise.

The results show that the finite element method was successfully used to solve the static contact problem. Both Hertzian and non-Hertzian contact problems were analyzed correctly. However, the application of the finite element method to the rolling contact problem was not completely successful. The finite element method results for tangential contact forces were about 25 percent lower than forces predicted by Kalker's theory. Recommendations for extending the analysis to solve the rolling contact problem are made. The report includes a derivation of the wheelset steady-state equations of motion, as well as a solution algorithm for the nonlinear, algebraic equations.

Acknowledgements

I would like to thank Dr. Robert H. Fries for serving as my adviser and for his guidance in my research work. Dr. Fries gave me much latitude in deciding how to conduct my work, and was always helpful in getting me through the rough spots. His knowledge and insight were invaluable in the completion of this work. I would also like to thank Drs. Charles E. Knight and Robert G. Leonard for serving on my Graduate Committee. Dr. Knight deserves special thanks for his help with the ABAQUS finite element program. This work could not have been completed without his expertise in the finite element method.

This work was partially funded by a grant from the Virginia Center for Innovative Technology. The ABAQUS finite element program was made available through an educational license from Hilbert, Karlsson and Sorenson. I would like to thank the consultants at HKS. Mr. Mark Bohm was especially patient in helping me unravel the mysteries of ABAQUS.

The consulting staff of the User Services Department at Virginia Tech also deserves credit for its excellent work. I owe a great deal of thanks to Mr. Burt Avery for his help with ABAQUS. His knowledge of the IBM mainframe operating systems was invaluable in solving some very difficult problems encountered while using ABAQUS. Mr. Avery was extremely patient and generous with his time.

I would like to express my gratitude to my fellow graduate students for their friendship. I would especially like to thank Mr. Robert (Wild Man) Williams for introducing me to the beautiful hiking around Virginia Tech. Thanks also to all the other wonderful people in the Mechanical Engineering Department.

Messrs. , and Mrs. deserve special thanks for proofreading my thesis. Their helpful comments and editing made this document a better work. Thanks are due also to Mr. V. Arun and Michelle for their help in preparing the figures which appear in this thesis. Finally, I would like to thank Michelle for her help in typing.

I would like to thank my parents, , for their love and support. They have shown me through their example that one can make one's dreams come true. I would also like to thank my parents-in-law, , for giving me a "home away from home". They and everyone else at the Anderson spread made me feel welcome and a part of their wonderful family.

My deepest thanks and gratitude go to my wife, , for her love and encouragement throughout our marriage. She has made many sacrifices and has been unselfish in giving me the time to pursue my studies. Thank you for making this all possible-- I love you very much.

Table of Contents

List of Illustrations

Chapter 1

Introduction

1.1 Background

The performance of rail vehicles on curved track has been studied for over fifty years. During curve negotiation, the performance of rail vehicles degrades significantly: fuel consumption is increased due to increased rolling resistance; the rate of wear of the wheels and rail is accelerated; the potential danger of derailment increases; and the objectionable noise associated with flanging occurs.

Much of the work done in the study of rail vehicle dynamics during curve negotiation has focused on steady-state curving. The assumption for steady-state curving is that the vehicle negotiates a constant radius curve at a constant velocity. Thus the transient dynamic behavior associated with curve entry quickly reaches steady-state.

In steady-curving analysis, the time varying terms of the vehicle differential equations of motion vanish. Then the equations of motion reduce to a set of nonlinear, algebraic equations. These equations can be solved readily by a nonlinear equation solver, such as Newton's method for several variables.

Many sophisticated models have been developed to solve the steady-state curving problem. These models include nonlinear suspension elements, rail lateral flexibility, and two-point wheel/rail contact. However, steady-state curving models generally use Kalker's method (1967) to characterize the wheel/rail contact forces. Kalker's work in the wheel/rail contact mechanics field has been widely used by the rail industry for the past 20 years.

Kalker's solution assumes that the wheel and the rail surfaces at the point of contact have constant curvature. This geometry is referred to as Hertzian contact geometry. This assumption is generally valid when the wheel and rail are new. Figure 1 shows that both the wheel and rail profiles are made up of sections of constant radius. However, after the wheel and rail are in service, they begin to wear. The curvature of the worn wheel and rail profiles are generally no longer constant. Thus the assumption of Hertzian contact geometry is invalid for worn wheels and rails.

Also, during curve negotiation, the wheelsets undergo large lateral motion relative to the rail. The result is that the point of contact on the wheel is at or near the wheel flange. As shown in Figure 1, the curvature of the wheel surface in this region changes rapidly. Here again, the assumption of Hertzian contact geometry is invalid.

The purpose of the work reported here was to investigate the effect of non-Hertzian contact geometry in the steady-state curving analysis. The finite element method

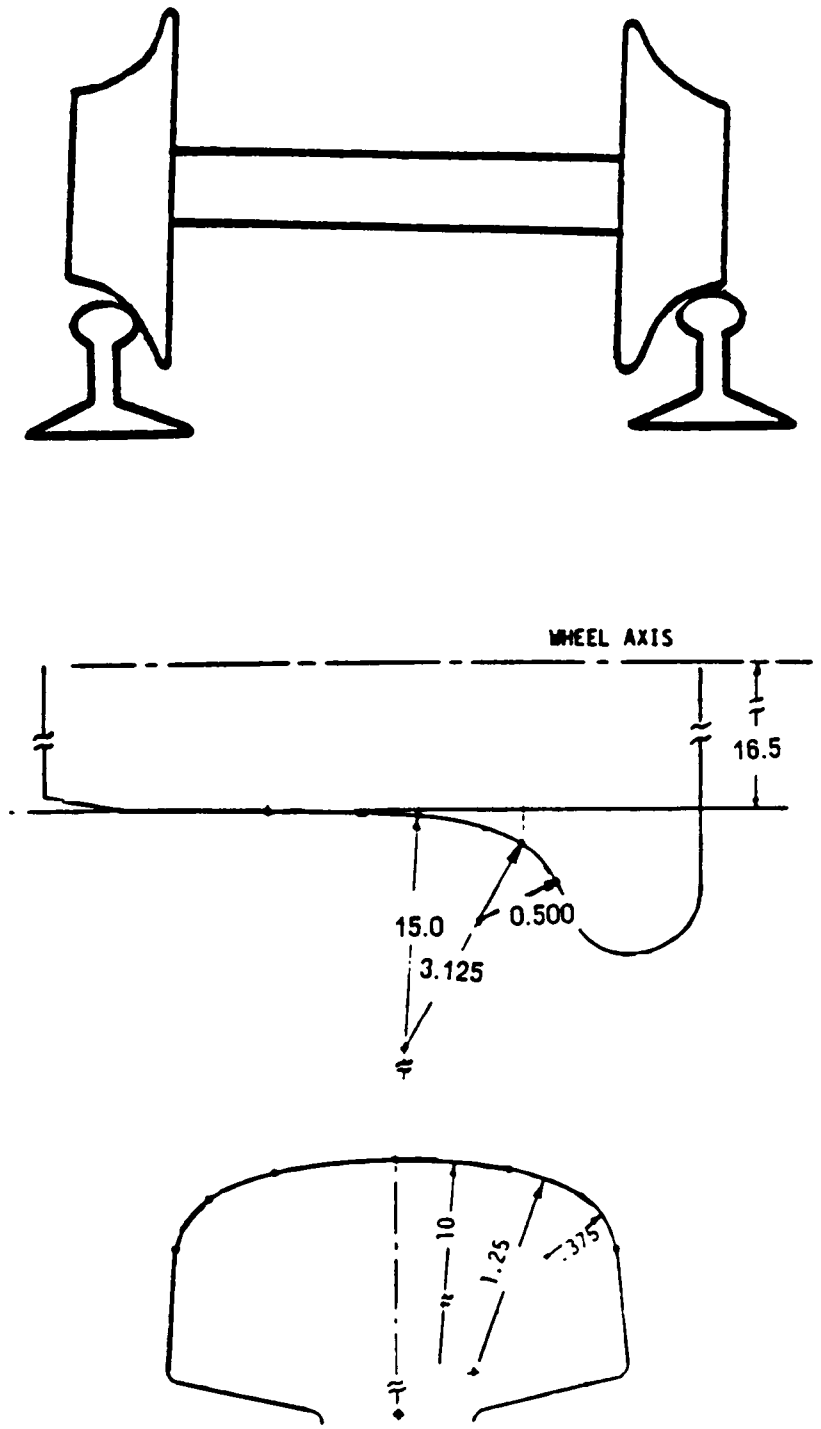

Figure 1. Typical New Wheel and Rail Profiles.

was investigated as a method to compute the wheel/rail contact forces. This method can account for the non-Hertzian geometry effects in the creep forces. Thus, the method has the potential to yield improved results in the analysis of worn wheels and rails, and in the curving analysis.

1.2 Related Literature

The earliest works in rail vehicle curving analysis assumed steady-state curving (Heumann, 1931 and Porter, 1935). These works were for rigid frame vehicles in tight curves. In these analyses, the flange and friction forces dominated the vehicle behavior. These early models lacked a correct treatment of the shear forces that develop when a wheel rolls with slip.

The relationship between slip and shear forces was established by Vermeulen and Johnson (1964). Kalker (1969) developed a linear contact theory that allowed for the calculation of the wheel/rail shear, or creep, forces. He later developed nonlinear theories that included the effects of creep force saturation to the adhesion limit (Kalker, 1979). Kalker's early contact theories are all based on Hertzian contact geometry.

The present day rail vehicle curving models are based on the classical work of Boocock (1969) and Newland (1969). These works developed a simplified linear theory for steady-state curving. In this theory, steering was provided by the creep forces in conjunction with the wheel conicity. The theory demonstrated that steering could

be achieved without flange contact. These theoretical models were limited due to linearization. The results were valid only for large radius curves.

The linear theory was extended to include nonlinear effects. Elkins and Gostling (1977) advanced a theory that included the effects of the real cross-sectional geometry of the wheel and rail. Their model also included the saturation of the creep forces to the adhesion limit, and their results were verified experimentally. Elkins and Eickhoff (1979) extended this analysis to include traction and braking torques. They also reported excellent agreement with experimental results.

These steady-state curving models assumed that each wheel made contact at a single point on the rails. However, two-point flange contact can occur during curving for many wheel and rail profiles. Marcotte, et al. (1981) used a simplified wheel profile to account for the possibility of two-point contact. The profile was represented by two different conical surfaces to model the tread and flange. Nagurka, et al. (1982) developed a sophisticated model to analyse curving with two-point contact. Their model included the effects of the real wheel geometry, rail flexibility, and a nonlinear creep force theory. Law, et al. (1986) used essentially the same scheme in their analysis of the steady-state curving behavior of locomotives.

More recently, research has been conducted on the dynamic analysis of rail vehicles in curves. These analyses are concerned with the transient behavior of the vehicle in curve entry and exit, where the track transitions from tangent track to curved track. Cooperrider and Law (1981) used a nonlinear, single-point contact vehicle model in their study. Their results indicated that transient wheel/rail forces could develop that were larger than predicted by the steady-state analysis. In some cases, the dynamic variations persisted in the steady curve, and the steady-state condition was never

reached. Nagurka, et al. (1984) used a nonlinear, two-point contact wheelset model to study dynamic curving. Their results also indicated the presence of transient wheel/rail forces that exceeded the steady values. However, their results approached steady values and substantiated the predictions of the steady-state analysis.

All of the modern curving theories discussed here utilize one of Kalker's creep force laws. These laws are based on Hertzian contact geometry, i.e., that the contact patch is elliptical. This assumption is invalid for wheel contact near the flange. The assumption is also incorrect for worn wheel and rail profiles. Thus it is of interest to investigate other methods of computing the creep forces.

Finite element methods have been developed that are capable of solving the general problem of two bodies in contact. The basic condition of contact is that no material overlap can occur between the two bodies. Two approaches are used to satisfy this condition. In the first approach, displacement constraints are imposed directly on the governing equations. Bathe and Chaudhary (1985) used this approach in developing a solution algorithm for planar and axisymmetric contact problems. Their algorithm allowed for frictional sliding according to a Coulomb friction law. The contact conditions were imposed using the total potential of the contact forces with the geometric compatibility conditions. This leads to an extra system of equations involving the contact nodes. The second approach to satisfy the impenetrability condition is to use "gap" elements to couple possible areas of contact. Simons and Bergan (1986) used this approach to develop a three-dimensional gap element for modelling contact with slip and friction. The element uses a stiffness formulation to transfer forces and model Coulomb friction.

1.3 Objectives

Solving the wheel/rail contact mechanics problem is the basis for studying rail vehicle dynamics. This thesis investigates the effect of non-Hertzian contact geometry on the rail vehicle steady-state curving solution. The finite element method is used to model the wheel/rail interaction.

There are three major objectives for this study:

1. Investigate the non-Hertzian contact problem using the finite element method. Develop efficient pre- and post-processing algorithms for solving the contact mechanics problem.

2. Derive the governing equations of motion for a rail vehicle on curved track. The equations of motion should be valid for two regions of vehicle motion: single-point wheel/rail contact and two-point wheel/rail contact (flanging).

3. Solve the steady-state equations of motion. Compare the results obtained using the finite element method to results published in the literature.

1.4 Organization of the Report

The remainder of this thesis is divided into five chapters. Chapter 2 contains a discussion of the mechanics of wheel/rail contact. Hertz's solution to the general con-

tact problem is presented, as well as Kalker's solution to the rolling contact problem. Then the finite element method solution for two bodies in contact is discussed.

Chapter 3 contains a derivation of the equations of motion for a rail vehicle on curved track. The steady-state equations are obtained from the governing differential equations. The equations of motion include the possibility of two-point contact.

The finite element analysis of the creep forces is discussed in Chapter 4. The finite element model and analysis technique are presented. Several illustrative examples are included.

An algorithm for solving the nonlinear, algebraic equations of motion is presented in Chapter 5. The solution method is based on Newton's method in several variables.

The report is summarized, and conclusions and recommendations for future research are presented in Chapter 6.

Chapter 2

Contact Mechanics of the Wheel/Rail Interface

When two bodies come into contact, they will generally touch at one or more points. If the two bodies are rigid, then the location of contact can be represented by a point of infinitesimally small area. However, if the bodies are elastic, then some deformation occurs around the point of contact. This creates a finite area of contact between the two bodies. This area is referred to as the contact patch.

The subject of contact mechanics deals with the deformation and resulting forces of two bodies in contact. Two types of forces act in the contact patch: normal forces and shear forces. The normal forces transmit any normal load between the two bodies. The shear forces are present when relative motion occurs between the two bodies. The limiting value of the shear force is μN : the coefficient of friction multiplied by the normal load.

The shear forces are of particular importance in solving the rail vehicle dynamics problem. These forces appear as generalized forces in the vehicle equations of mo-

tion. Thus, the solution of the contact problem is closely related to the solution of the vehicle motion. It is necessary to accurately determine the shear forces in order to correctly solve the equations of motion.

This chapter discusses the solution of the contact patch mechanics problem. The wheel/rail kinematics problem is discussed first. Hertz's solution to the static contact problem is presented next. Hertz solved the contact problem for two curved bodies with constant curvature. This class of problems is referred to as Hertzian contact geometry. Then, Kalker's solution to the rolling contact problem is discussed. Kalker's work is based on Hertz's solution, and is restricted to Hertzian contact geometry. Kalker allows for relative motion between the two contacting bodies. Finally, a finite element solution method to the contact problem is presented. The finite element method can solve any geometrically admissible contact problem, and can allow for relative motion between the contacting bodies.

2.1 Wheel/Rail Kinematics

The contact mechanics problem is strongly dependent on the shape of the two bodies in the vicinity of contact. The profiles of the wheel and rail are usually known. Then the contact geometry can be determined by finding the point of contact on each body and the relative rotation between the bodies. Thus to solve the contact problem one must be able to :

- determine the initial point of contact on the wheel and rail

- determine the geometry of the two bodies at this point.

Cooperrider, et al. (1975) developed the FORTRAN program WHRAIL to solve this kinematics problem. In WHRAIL, the wheelset and rail are treated as rigid, inelastic bodies that lie in a vertical plane. As a planar rigid body, the wheelset has three degrees of freedom. When the wheelset contacts the two rigid rails, two constraints are provided. Then, the wheelset planar motion can be completely defined by the lateral displacement. The wheelset roll angle and vertical displacement are constrained variables. The WHRAIL program determines the wheel/rail contact positions and the wheelset roll angle as a function of the wheelset lateral displacement. Figure 2 shows sample output from the WHRAIL program. This example uses a new 33-inch Canadian National A (CNA) wheel profile with a new 132-lb American Railway Engineering Association (AREA) rail.

The WHRAIL program provides the necessary information to specify the contact geometry: the wheel/rail contact positions and the wheelset roll angle. This program also produces other valuable data which will be used later in this report. These include the wheel/rail contact angles, used in the derivation of the wheelset equations of motion in Chapter 3. Also, the creep force coefficients, used in the solution of the equations in Chapter 5.

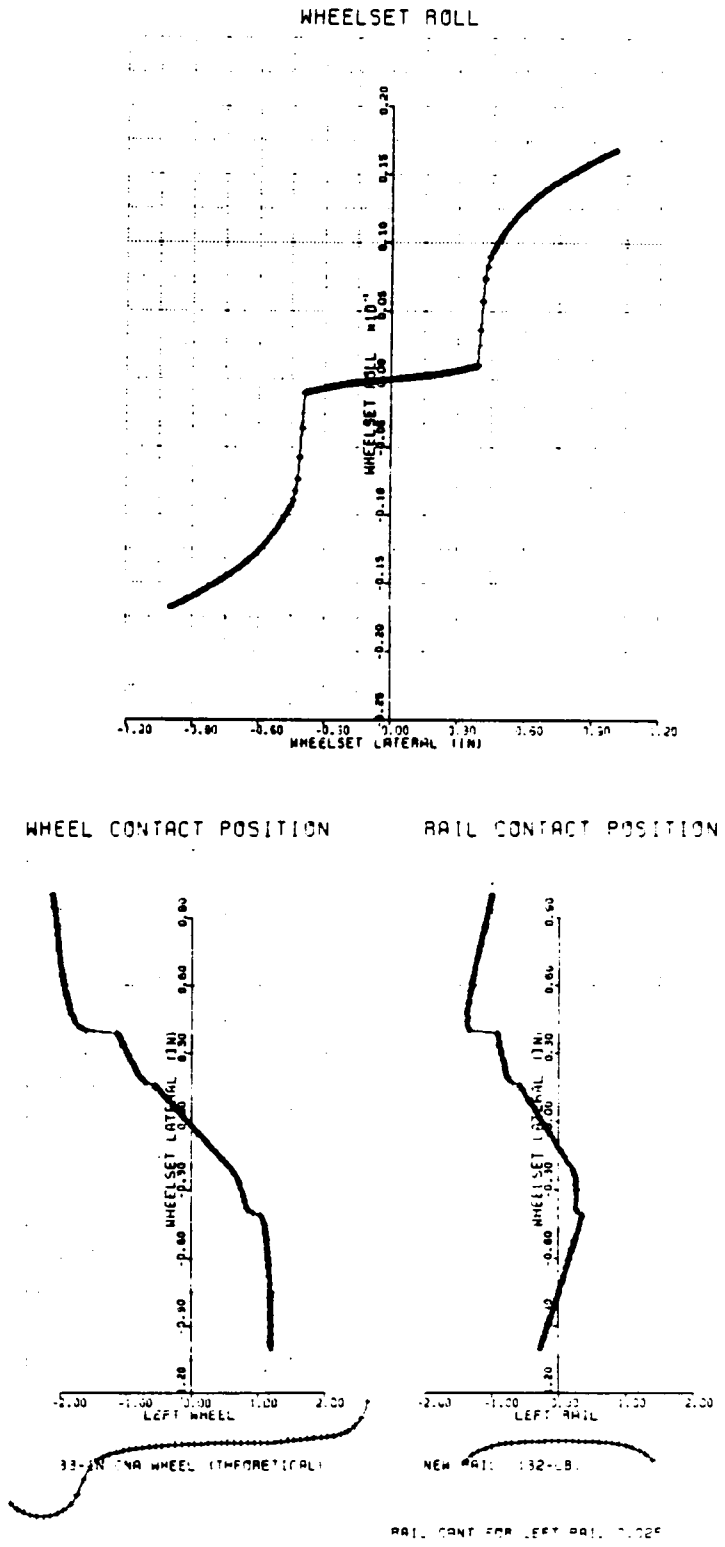

Figure 2. Roll Angle and Contact Location on Wheel and Rail

2.2 *Hertzian Contact Geometry*

Hertz was the first person to solve the problem of two elastic bodies in contact (see Figure 3). He worked on this problem while serving as an assistant to Helmholtz at Berlin in 1881. Hertz was 24 years old at the time.

Hertz's solution is based on assumptions of three types (Boresi, et al., 1978):

- material properties
- shape of the contact surface before loading
- shape of the contact surface after loading

The materials of the two bodies are assumed to be homogeneous, isotropic, and linearly elastic. It is not required that the two bodies be of the same material.

The bodies are assumed to be curved, with two principal radii of curvature (see Figure 3). The radii of curvature are constant near the point of contact. When the two bodies contact, they share a common normal which is perpendicular to a plane tangent to the point of contact. Then the distance between corresponding points on the two bodies can be approximated by (Boresi, et al., 1978):

$$z = Ax^2 + By^2 \qquad [2.1]$$

The locus of points with constant z is shown in Figure 4a. The parameters A and B are given by Boresi, et al. (1978):

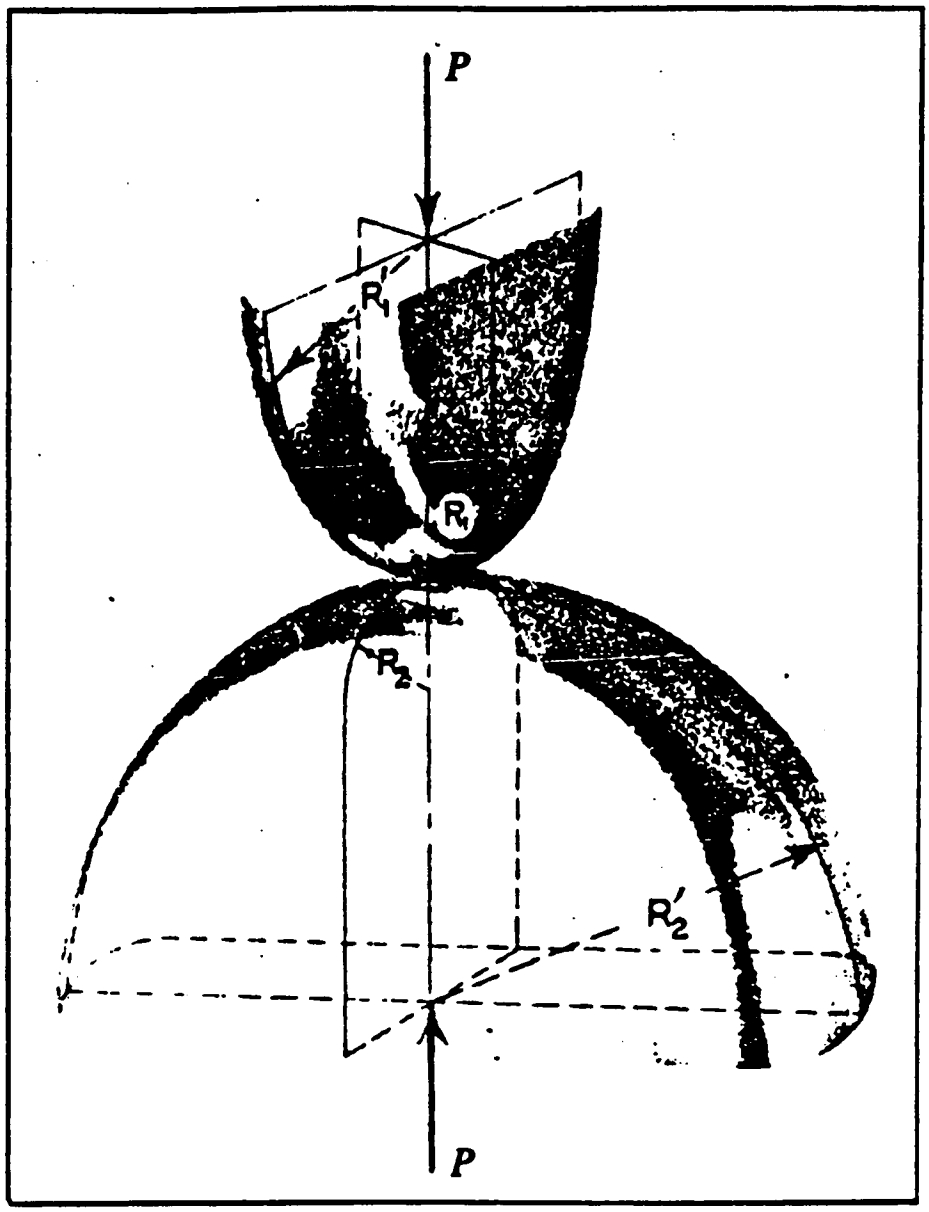

Figure 3. Hertzian Contact Problem (Boresi, et al., 1978)

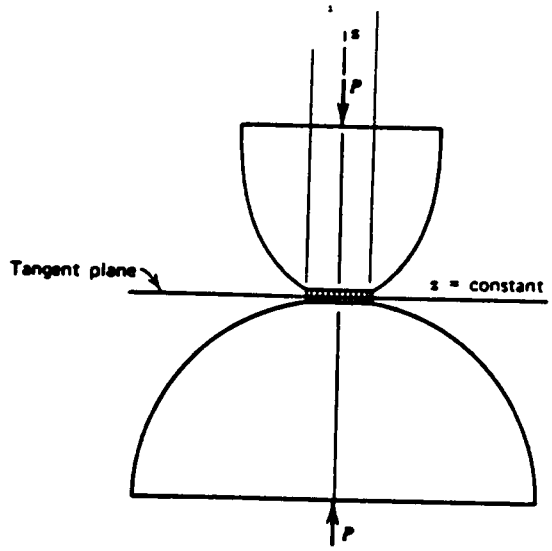

Before Loading

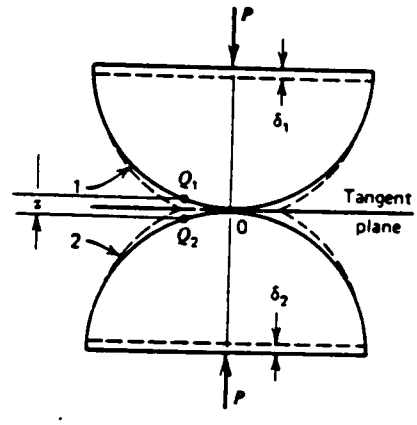

After Loading

Figure 4. Geometry of Bodies Before and After Contact (Boresi, et al., 1978)

$$A = \frac{1}{2}\left(\frac{1}{R_1} + \frac{1}{R_2}\right) \qquad [2.2a]$$

$$B = \frac{1}{2}\left(\frac{1}{R'_1} + \frac{1}{R'_2}\right) \qquad [2.2b]$$

After loading, it is assumed that points that come into contact were originally equidistant from the tangent plane. From equation 2.1, the locus of points with constant distance z from the tangent plane lie on an ellipse. Thus the boundary of the contact area is assumed to be an ellipse, given by (Boresi, et al., 1978):

$$\frac{x^2}{a^2} + \frac{y^2}{b^2} = 1 \qquad [2.3]$$

The constants a and b are the semi-radii of the contact ellipse.

After the load is applied, points far removed from the contact area move closer by a distance $\delta = \delta_1 + \delta_2$ (see Figure 4b). This distance is referred to as the approach. Points close to the contact area experience local compression effects. The variable w_1 is defined as the deformation of point Q_1 on body 1 due to local compression, and w_1 is defined positive away from the tangent plane. Similarly, w_2 is the deformation of point Q_2 on body 2 due to local compression effects, and w_2 is defined positive away from the tangent plane. Then the two corresponding points Q_1 and Q_2 move closer by the amount $\delta - (w_1 + w_2)$. If the points Q_1 and Q_2 are within the contact ellipse, their deformation is equal to their initial separation. This is given by:

$$\delta - (w_1 + w_2) = z_1 + z_2 = z \qquad [2.4]$$

The initial separation z is defined by equation 2.1. Substituting equation 2.1 into equation 2.4 and solving for $(w_1 + w_2)$ yields:

$$w_1 + w_2 = \delta + Ax^2 + By^2 \qquad [2.5]$$

Equation 2.5 is the governing equation for the contact problem: the local deformation is specified in terms of the load (approach) and the global coordinates. Hertz noted that equation 2.5 had the same form as that of the Newtonian potential equation for the attraction of an ellipsoid upon a point mass. This Newtonian potential function satisfies the same differential equations that are required by the theory of elasticity. The contact problem is solved by substituting into this potential function the stresses at the contact surface instead of the mass, etc. (Boresi, et al., 1978).

The solution for the stress and deflection field are in terms of the elliptic integrals. These integrals must be evaluated numerically or be found using a lookup table. Thus the exact equations for the contact stresses and approach are difficult to employ.

Alternatively, a graphical method based upon previously computed elliptic integrals can be used to facilitate the solution of the contact problem. In this method the elliptic integrals are replaced by constants. The constants are graphed as a function of the geometry parameter $\frac{B}{A}$. This method will be used in Chapter 4 to verify the finite element results for the contact problem. The equations used in the verification are summarized below for reference (Boresi, et al, 1978).

The semi-radii of the contact ellipse are given by:

$$a = \frac{1}{k}b$$
$$b = c_b\sqrt[3]{P\Delta} \qquad [2.6]$$

where

$$\Delta = \frac{1}{A + B}\left(\frac{1 - \nu_1^2}{E_1} + \frac{1 - \nu_2^2}{E_2}\right)$$

$E_{1,2}$ = Young's modulus for bodies 1 and 2, respectively

$\nu_{1,2}$ = Poisson's ratio for bodies 1 and 2, respectively

The constants k and c_b are plotted in Figure 5 as a function of $\frac{B}{A}$.

The maximum principal stress is the stress normal to the tangent plane at the center of the contact ellipse. It is given by:

$$\sigma_{max} = c_\sigma\left(\frac{b}{\Delta}\right) \qquad [2.7]$$

The constant c_σ is plotted in Figure 5 as a function of $\frac{B}{A}$.

The maximum shearing stress is given by:

$$\tau_{max} = c_\tau\left(\frac{b}{\Delta}\right) \qquad [2.8]$$

The maximum octahedral shearing stress is given by:

$$\tau_{oct} = c_g\left(\frac{b}{\Delta}\right) \qquad [2.9]$$

The maximum shearing stress τ_{max} occurs inside the body some distance from the center of the contact ellipse. This distance z_s is:

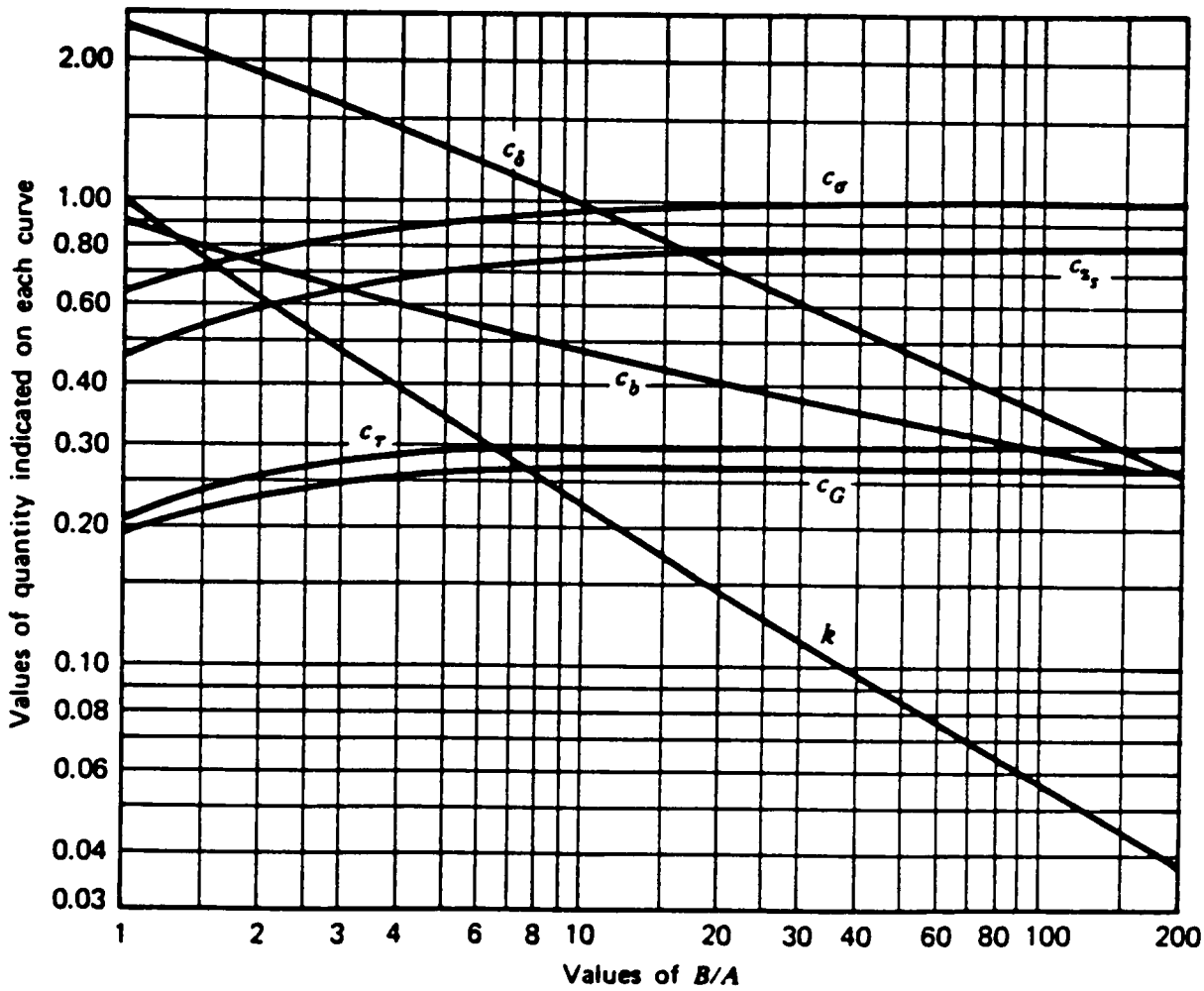

Figure 5. Stress and Deflection Factors for Hertzian Contact Problem (Boresi, et al., 1978)

$$z_s = c_{zs} b \qquad [2.10]$$

The constants c_τ , c_φ, and $c_{z\varphi}$ are shown in Figure 5 as a function of $\frac{B}{A}$.

2.3 Rolling Contact Force Model

The important phenomenon of a wheel rolling with creepage is introduced in this section. Creepage, or slip, is defined as the relative velocity between the wheel and the rail in the contact patch divided by the speed of the contact patch. Creepage gives rise to creep forces acting on the wheel. The creep forces govern the behavior of the wheel, and thus the vehicle. In the following, creepage and creep force models are examined.

A wheel rolling on a surface can exhibit three states of slip, as shown in Figure 6. In the first case shown in the figure, the wheel rolls "perfectly". Thus every part of the wheel in the contact patch adheres to a corresponding point on the surface. There is no relative velocity between the wheel and the surface. Thus no creep forces are generated in the contact patch.

In the second case shown in Figure 6, part of the wheel in the contact patch adheres to the surface while the rest of the wheel slips. An example of this case occurs when the vehicle is accelerating or braking. The resulting creep forces are traction and braking forces, respectively. Another example is a rail vehicle on curved track. The

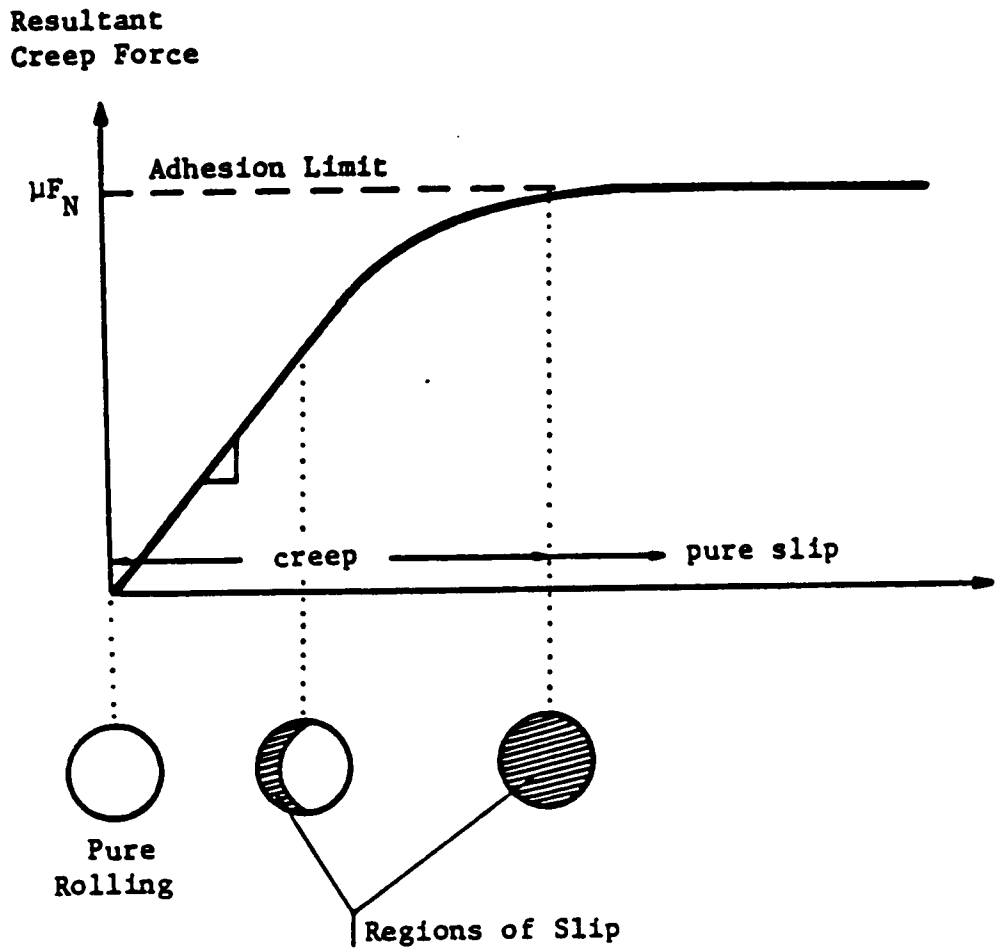

Figure 6. Three States of Slip in Contact Patch (Nagurka, 1983)

wheelset in this case develops large creepages. The resulting creep forces act to balance the centrifugal forces on the wheelset.

In the third case shown in Figure 6, the entire wheel in the contact patch slips relative to the surface. An example of this case occurs when the vehicle is braking and the wheels lock. Then the wheel slides on the surface; no point on the wheel in the contact patch adheres to the rail. Another example of this case occurs in severe curving where flanging occurs. Then the wheel flange slips relative the rail head. The creep forces generated in both these examples are saturated friction forces, μN.

Most of the current research in rail vehicle dynamics relies on Kalker's creep force models. Kalker's theories include the linear theory, the simplified theory and the "exact" numerical theory (Shen, et al., 1983). In the linear theory, the creep force is linearly proportional to the the creepage. In the simplified theory, the tangential traction is proportional to the tangential displacements. This model is incorporated in the computer program FASTSIM. The "exact" numerical solution is incorporated in the computer program DUVORAL.

The linear creep theory is the most convenient for dynamic analysis. This theory relates the creep forces and moments to the creepages as follows (Davila, 1986):

$$\begin{aligned} F_{LA} &= c^2 G C_{22} \zeta_{LA} + c^3 G C_{23} \zeta_{SP} \\ F_{LO} &= c^2 G C_{11} \zeta_{LO} \\ M_{SP} &= -c^3 G C_{23} \zeta_{LA} + c^4 G C_{33} \zeta_{SP} \end{aligned} \qquad [2.11]$$

where,

F_{LA} = lateral creep force

F_{LO} = longitudinal creep force

M_{SP} = spin creep moment

ζ_{LA} = lateral creepage

ζ_{LO} = longitudinal creepage

ζ_{SP} = spin creepage

C_{ij} = Kalker's nondimensional creep coefficients

G = combined modulus of rigidity

$$= \frac{2}{1/G_1 + 1/G_2}$$

c $= \sqrt{ab}$

G_1 and G_2 are the shear moduli of bodies 1 and 2, respectively. a and b are the semi-radii of the contact ellipse found by Hertz's solution. The creep forces in equation 2.11 can be expressed in matrix form:

$$\begin{bmatrix} F_{LA} \\ M_{SP} \\ F_{LO} \end{bmatrix} = - \begin{bmatrix} F_{11} & F_{12} & 0 \\ -F_{12} & F_{22} & 0 \\ 0 & 0 & F_{33} \end{bmatrix} \begin{bmatrix} \zeta_{LA} \\ \zeta_{SP} \\ \zeta_{LO} \end{bmatrix} \qquad [2.12]$$

where,

$F_{11} = -c^2GC_{22}$

$F_{12} = -c^3GC_{23}$

$F_{22} = -c^4GC_{33}$

$F_{33} = -c^2GC_{11}$

The major drawback of the linear theory is that it does not include the friction saturation effect, $F \leq \mu N$. In a curving analysis this effect is very important. Large creepages develop resulting in saturated creep forces. Shen (1983) includes a survey of three creep force models that provide for saturation. These are Kalker's simplified

theory and "exact" theory, and a "Heuristic" nonlinear creep force model. The saturation characteristics of these three models are compared in Figure 7. In the next section, the finite element method is discussed as an alternative solution to the creep force problem.

2.4 Finite Element Method Contact Model

This section provides a brief overview of how the contact conditions are determined by the finite element method. The finite element theory is well documented in the literature (Bathe, 1982 and Reddy, 1984). It is beyond the scope of this report to do an in-depth study of the finite element theory. Thus this section is limited to the formulation of the contact problem. The solution algorithm incorporated in the ABAQUS finite element program is described.

In the finite element method, the geometry of the two bodies in contact is defined by a mesh of nodes. The external forces acting on the bodies and the displacement boundary conditions are specified with respect to these nodes. The two bodies are referred to arbitrarily as the contactor body and the target body (see Figure 8a).

The basic condition of contact along the contact surfaces is that no material overlap can occur (see Figure 8b). When overlap is detected, contact forces develop in the region of contact (see Figure 8c). These forces act upon the two bodies to remove the overlap. This procedure is performed iteratively until an equilibrium solution is reached.

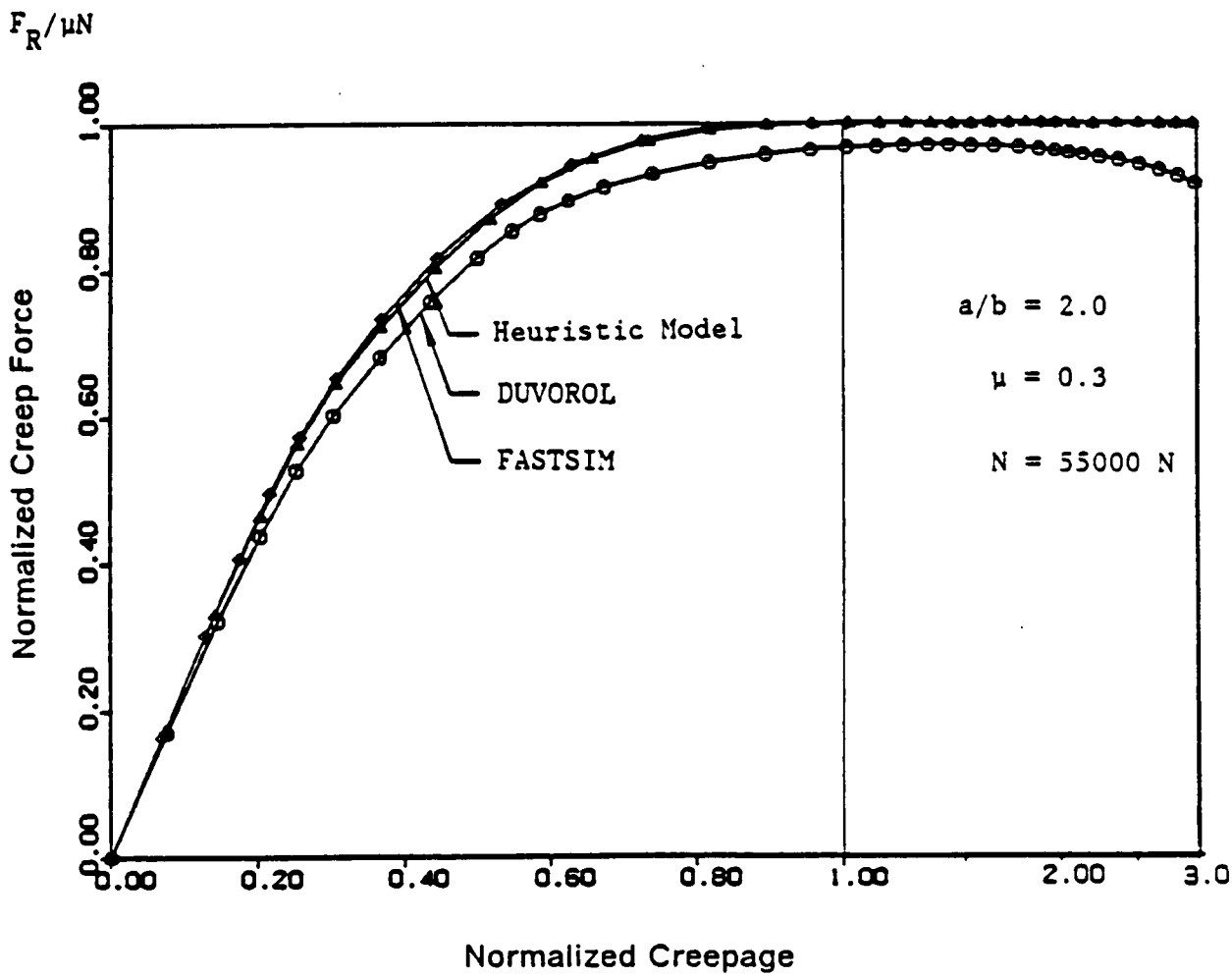

Figure 7. Saturation Characteristics of Different Creep Force Models (Davila, 1986)

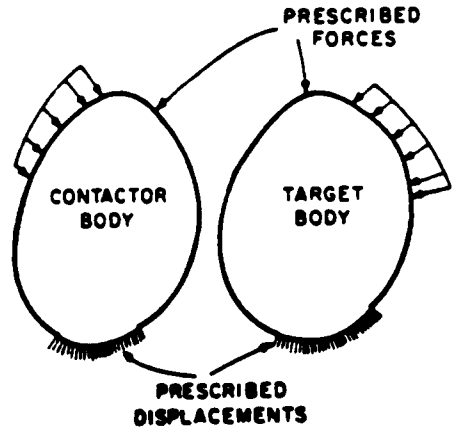

(a) Condition prior to contact

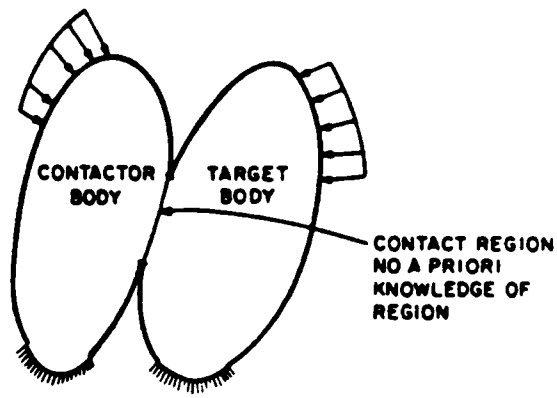

(b) Condition at contact

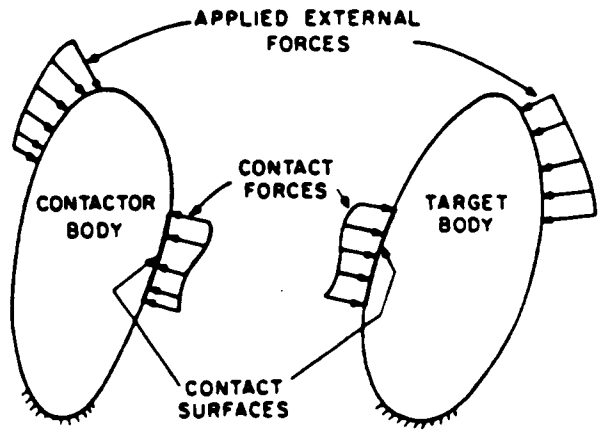

(c) Forces acting on contactor and target bodies

Figure 8. Schematic Representation of the Contact Problem (Bathe and Chaudhary, 1985)

There are two types of contact forces that act in the contact region: normal and tangential forces. The normal forces are compressive only; tensile normal forces are not permitted. The tangential forces satisfy a law of frictional resistance, usually the Coulomb law of friction (ABAQUS User's Manual, 1985).

The Coulomb law of friction is a simple 'stick-slip' friction model. It is characterized by the coefficient of friction, μ . The tangential force developed along the contact surface is denoted by $\underline{Q}$. There is no relative motion between two adjacent particles on the two bodies in contact as long as $|\underline{Q}| \leq \mu N$, where N is the compressive normal force. This is the 'stick' condition. Once $|\underline{Q}|$ exceeds μN , then the two particles move relative to one another. This is the 'slip' condition. Relative motion between two adjacent particles continues as long as the tangential force is developed to equal μN . Once the developed tangential traction drops below the friction limit, the relative motion between the adjacent particles stops.

The finite element contact equations are derived using a Lagrange multiplier method. With this method, an additional equation is generated for a node when contact is detected. A node is assumed to be in contact if one of two conditions is satisfied (ABAQUS User's Manual, 1985):

- the contactor node has penetrated the target body in the previous iteration

- the normal force acting at a node already in contact is positive.

In the first case, the contact force at the node at the beginning of the iteration is zero. The normal contact force is generated during the iteration when overlap is eliminated. The following constraint condition is introduced:

$$N(\Delta) = 0 \qquad [2.13]$$

where,

N = Lagrange multiplier; normal force at node in contact

Δ = overlap at node in contact

If the normal force is tensile, then the node is released from contact in the following iteration.

The differential strain measure for a node in contact can be decomposed into an elastic component and a sliding component (ABAQUS Theory Manual, 1984):

$$\begin{aligned} d\underline{\varepsilon} &= d\underline{\varepsilon}^{EL} + d\underline{\varepsilon}^{SL} \\ d\underline{\varepsilon} &= [d\varepsilon_3,\ d\gamma_1,\ d\gamma_2] \end{aligned} \qquad [2.14]$$

where,

ε_3 = normal strain measure, positive in compression

$\varepsilon_3^{SL} = 0$

$\gamma_{1,2}$ = tangential strain measure

The strain measure $d\underline{\varepsilon}$ is measured in a local coordinate system which may be rotating.

The tangential shear forces acting at a node in contact are defined by the following stiffness equation:

$$dQ_\alpha = G d\gamma_\alpha^{EL} \qquad \alpha = 1,2 \qquad [2.15]$$

where,

Q_α = shear forces

G = shear stiffness-in-stick coefficient

The shear forces are proportional to the elastic component of the strain measure. The magnitude of the shear forces cannot exceed the friction limit. Thus, the shear forces are subject to a yield condition which can be stated as:

$$(Q_1Q_1 + Q_2Q_2)^{\frac{1}{2}} - \mu N = 0 \qquad [2.16]$$

The shear forces defined above exhibit an elastic-perfectly plastic behavior, as shown in Figure 9. When the magnitude of the shear forces exceeds the friction limit, the contactor node slides relative to the target node. The sliding component of the strain measure is computed according to a flow rule given by:

$$d\gamma_\alpha^{SL} = d\lambda \frac{Q_\alpha}{\mu N} \qquad [2.17]$$

The term $d\lambda$ represents the rate of sliding of the node (ABAQUS Theory Manual, 1984 and HKS, 1987).

The algorithm for solving the nonlinear finite element equations can be summarized as follows (HKS, 1987):

1. update the stiffness matrix and loads

2. compute displacements; compute overlap at contact element nodes

3. compute strains

4. compute stresses

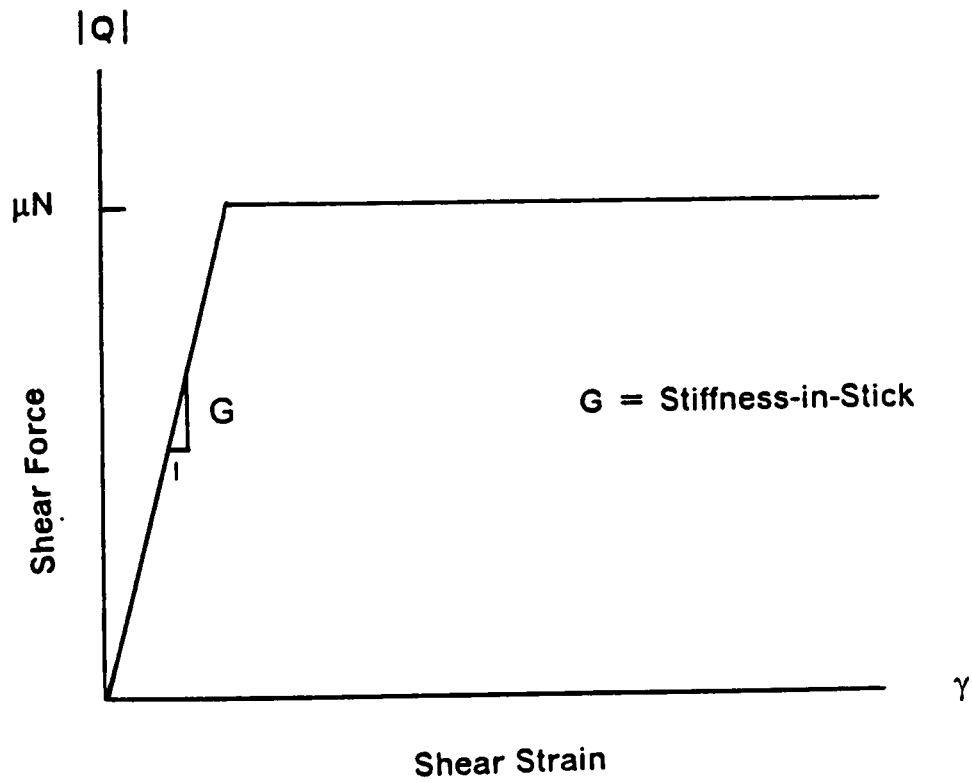

Figure 9. ABAQUS Shear Force Constitutive Law

5. check equilibrium

These steps are repeated iteratively until equilibrium is satisfied to within a specified tolerance.

2.5 Summary

In order to solve the wheelset curving problem, it is necessary to:

- solve the wheel/rail kinematic constraint problem
- determine the wheel/rail contact forces

This chapter discussed methods for solving the above two tasks. First, the WHRAIL program was presented as a means for solving the kinematic constraint problem. WHRAIL determines the various wheel/rail constraint variables as a function of the wheelset lateral displacement. Next, Hertz's solution to the static contact problem was discussed. His solution was for two curved bodies with constant curvature. Finally, two methods for solving the rolling contact problem were presented. Kalker's theories are based on Hertzian contact geometry. The finite element method can be used to solve any geometrically admissible contact problem. In Chapter 4, the finite element method is used to solve the static and rolling wheel/rail contact problem. Kalker's linear theory is used in Chapter 5 to solve an example curving problem.

Chapter 3

Wheelset Mechanics During Curving

The wheelset is the most important component of any rail vehicle model. The interaction of the vehicle and the track is accounted for in the wheelset model. Thus the wheelset merits special study.

The equations of motion for a wheelset on curved track are derived in this chapter. The equations are obtained using Newton's Second Law of Motion and Euler's Equations. The steady-state equations of motion are found from these differential equations.

3.1 Wheelset Reference Frames

The coordinate systems used to derive the governing equations are shown in Figure 10. In this figure, a wheelset is shown traversing a curve of radius R with constant velocity V. There is an inertial reference frame, {n}, fixed at the center of the curve, point 'O'.

The reference frame {a} is a rotating frame whose origin is at point 'O'. Reference frame {a} follows the wheelset as it traverses the curve. Thus the a_1 axis remains pointed at the wheelset center of mass. The frame has an angular velocity of $\underline{\omega}^A = -\frac{V}{R}\hat{\underline{a}}_2$.

The reference frame {t} is aligned with the track. The origin of {t} moves along the track centerline as {t} rotates with frame {a}. The two reference frames have the same angular velocity: $\underline{\omega}^T = \underline{\omega}^A$.

The components of {t} can be expressed in terms of {a}. The transformation is given by:

$$\{t\} = [R_3(\varphi_{SE})]\{a\} \qquad [3.1]$$

where $[R_3(\varphi_{SE})]$ is the transformation matrix

$$[R_3(\varphi_{SE})] = \begin{bmatrix} \cos\varphi_{SE} & \sin\varphi_{SE} & 0 \\ -\sin\varphi_{SE} & \cos\varphi_{SE} & 0 \\ 0 & 0 & 1 \end{bmatrix} \qquad [3.2]$$

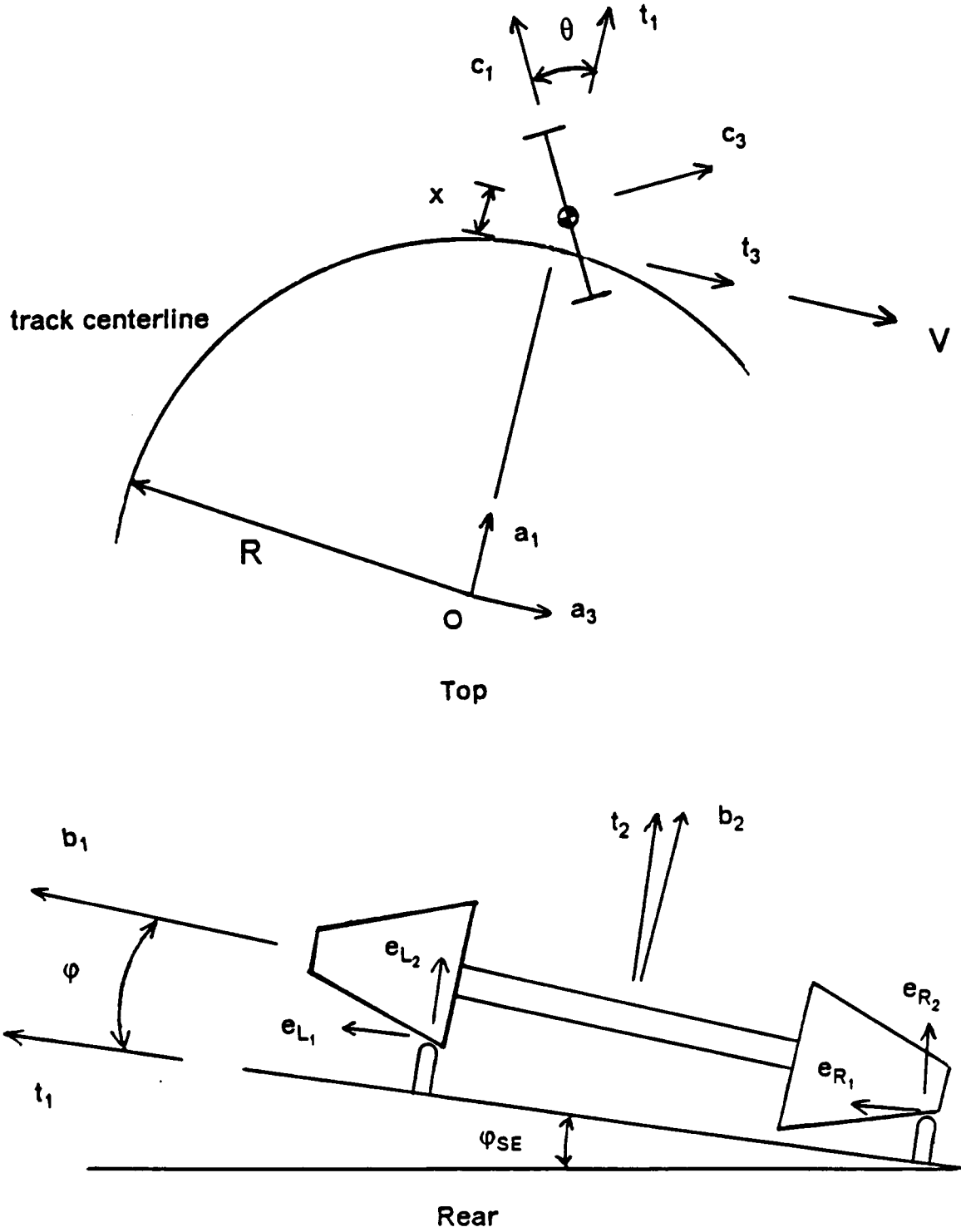

Figure 10. Reference Frames for Wheelset on Curved Track

The angle φ_{SE} is the superelevation angle.

The reference frame {c} is a rotating frame whose origin is at the wheelset center of mass. The reference frame {c} is rotated by an angle θ from the {t} frame. This rotation is the wheelset "yaw". The reference frame {c} has an angular velocity of $\underline{\omega}^C = \dot{\theta}\,\hat{\underline{c}}_2 + \underline{\omega}^T$.

The components of {c} can be expressed in terms of the {t} frame. The transformation is given by:

$$\{c\} = [R_2(\theta)]\{t\} \qquad [3.3]$$

where $[R_2(\theta)]$ is the transformation matrix

$$[R_2(\theta)] = \begin{bmatrix} \cos\theta & 0 & -\sin\theta \\ 0 & 1 & 0 \\ \sin\theta & 0 & \cos\theta \end{bmatrix} \qquad [3.4]$$

The reference system {b} is aligned with the wheelset and fixed at the wheelset center of mass. The b_1 axis coincides with the wheelset axis of revolution. The reference frame {b} is rotated by an angle φ from the {c} system. This rotation is the wheelset "roll". Thus, the reference system {b} has an angular velocity $\underline{\omega}^B = \dot{\varphi}\hat{\underline{b}}_3 + \underline{\omega}^C + \underline{\omega}^T$.

The components of {b} can be expressed in terms of the {t} frame. The transformation is given by:

$$\{b\} = [R_3(\varphi)]\{c\} = [R_3(\varphi)][R_2(\theta)]\{t\} \qquad [3.5]$$

The usual approximation is that the yaw and roll angles are small (Nagurka, 1983). Then equation 3.5 becomes:

$$\{b\} = \begin{bmatrix} 1 & \varphi & -\theta \\ -\varphi & 1 & 0 \\ \theta & 0 & 1 \end{bmatrix} \{t\} \qquad [3.6]$$

The normal and tangential directions at the contact patch are specified by the contact patch axes. The reference frames $\{e_L\}$ and $\{e_R\}$ denote the contact patch axes for the left and right wheel, respectively. These frames are rotated from the the $\{t\}$ frame as shown below and in Figure 10.

$$\{e_L\} = [R_3(\varphi + \delta_L)]\{t\} \qquad [3.7a]$$

$$\{e_R\} = [R_3(\varphi - \delta_R)]\{t\} \qquad [3.7b]$$

The angles δ_L and δ_R are the contact angles at the left and right wheels, respectively. The contact angle is the angle between the plane of the contact patch and the axis of the wheelset.

3.2 *Single-Point Wheel/Rail Contact*

The free-body diagram for a wheelset on a curved track is shown in Figure 11. The creep forces and moment at the left and right wheel are denoted by $F_{LA_{L,R}}$, $F_{LO_{L,R}}$, and $M_{SP_{L,R}}$. The normal forces at the left and right wheels are denoted by N_L and N_R, re-

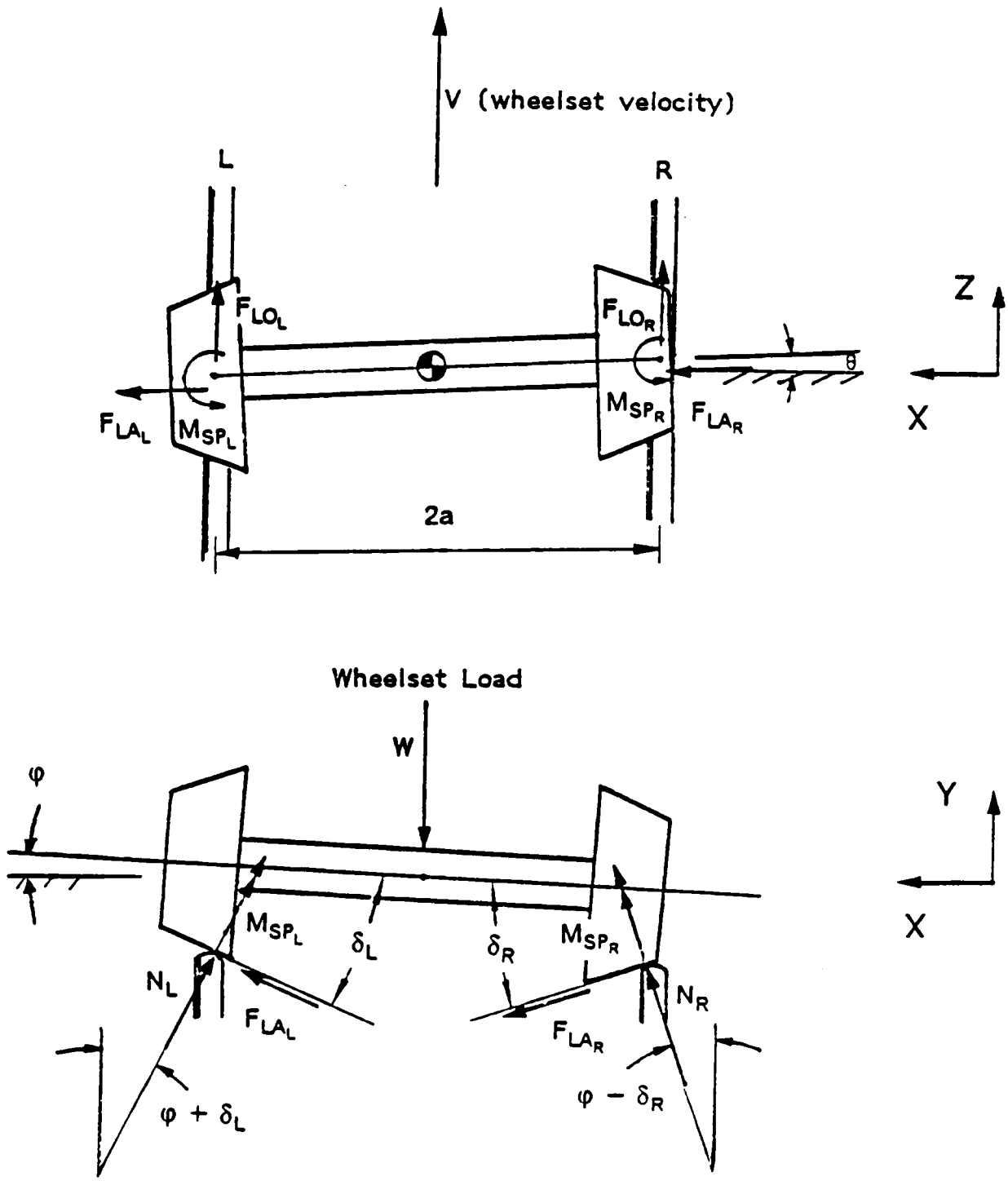

Figure 11. Free-Body Diagram for a Wheelset with Single-Point Contact

spectively. The normal forces are not known a priori and thus are treated as unknowns.

There are five unknowns in this problem: the lateral displacement, x; the yaw angle, θ ; the normal forces, N_L and N_R ; and the steady-state change in the spin angular velocity, $\dot{\beta}$. Five equations can be written to solve for the unknowns. These are:

- lateral equation $\sum_i F_{x_i} = m\ddot{x}$
- yaw equation $\sum_i M_{y_i} = I_{yy}\ddot{\theta}$
- vertical equation $\sum_i F_{y_i} = m\ddot{y}$
- roll equation $\sum_i M_{z_i} = I_{zz}\ddot{\varphi}$
- spin equation $\sum_i M_{x_i} = I_{xx}\ddot{\beta}$

In the following, each of the above equations is derived using Newton's Second Law of Motion or Euler's Equations.

Lateral Equation

From Figure 10, the position vector of the wheelset center of mass is given by:

$$\underline{r} = [R + x]\hat{\underline{a}}_1 \qquad [3.8]$$

The acceleration in the inertial reference frame is found by using the transport theorem to differentiate equation 3.8. The transport theorem is given by (Meirovitch, 1970):

$$\frac{{}^{N}d}{dt}(\underline{r}) = \frac{{}^{A}d}{dt}(\underline{r}) + \underline{\omega}^{A} \times (\underline{r}) \qquad [3.9]$$

The superscripts N and A refer to the inertial reference frame {n} and local reference frame {a}, respectively. Equation 3.8 is differentiated twice to yield the acceleration. The results are shown below, assuming $x << R$:

$$\dot{\underline{r}} = \frac{{}^{N}d}{dt}\underline{r} = \dot{x}\hat{\underline{a}}_{1} + V\hat{\underline{a}}_{3} \qquad [3.10]$$

$$\ddot{\underline{r}} = \frac{{}^{N}d}{dt}\dot{\underline{r}} = \left[\ddot{x} - \frac{V^2}{R}\right]\hat{\underline{a}}_{1} + 2\frac{V\dot{x}}{R}\hat{\underline{a}}_{3} \qquad [3.11]$$

The acceleration can be expressed in the {t} coordinate frame by making use of the transformation in equation 3.1. Assuming small angles, the acceleration is:

$$\ddot{\underline{r}} = \left[(\ddot{x} - \frac{V^2}{R})\right]\hat{\underline{t}}_{1} - \left[(\ddot{x} - \frac{V^2}{R})\varphi_{SE}\right]\hat{\underline{t}}_{2} + \left[2\frac{V\dot{x}}{R}\right]\hat{\underline{t}}_{3} \qquad [3.12]$$

The forces acting on the wheelset are shown in Figure 11. The contact forces are expressed in the contact patch reference frames:

$$\begin{aligned} &\text{Left Wheel} && \underline{F}_{L} = F_{LA_L}\hat{\underline{e}}_{1_L} + N_L\hat{\underline{e}}_{2_L} + F_{LO_L}\hat{\underline{e}}_{3_L} \\ &\text{Right Wheel} && \underline{F}_{R} = F_{LA_R}\hat{\underline{e}}_{1_R} + N_R\hat{\underline{e}}_{2_R} + F_{LO_R}\hat{\underline{e}}_{3_R} \end{aligned} \qquad [3.13]$$

These force vectors are transformed to the track axes {t} using equation 3.7. The resulting forces are:

$$\underline{F}_L = \left[F_{LA_L}\cos(\varphi + \delta_L) - N_L \sin(\varphi + \delta_L)\right]\hat{\underline{t}}_1 + \left[N_L \cos(\varphi + \delta_L) + F_{LA_L}\sin(\varphi + \delta_L)\right]\hat{\underline{t}}_2 + F_{LO_L}\hat{\underline{t}}_3 \qquad [3.14a]$$

$$\underline{F}_R = \left[F_{LA_R}\cos(\varphi - \delta_R) - N_R \sin(\varphi - \delta_R)\right]\hat{\underline{t}}_1 + \left[N_R \cos(\varphi - \delta_R) + F_{LA_R}\sin(\varphi - \delta_R)\right]\hat{\underline{t}}_2 + F_{LO_R}\hat{\underline{t}}_3 \qquad [3.14b]$$

The weight of the wheelset acts through the centroid: $\underline{F}_w = -mg\hat{\underline{a}}_2$. This gravitational force is transformed to the track axes using equation 3.1:

$$\underline{F}_W = -mg \sin\varphi_{SE}\hat{\underline{t}}_1 - mg\cos\varphi_{SE}\hat{\underline{t}}_2 \qquad [3.14c]$$

The lateral equation of motion is obtained by summing the forces in the t_1 direction and applying Newton's Second Law. Using equations 3.12 and 3.14, the lateral equation is:

$$m(\ddot{x} - \frac{V^2}{R}) = F_{LA_L}\cos(\varphi + \delta_L) + F_{LA_R}\cos(\varphi - \delta_R) - N_L \sin(\varphi + \delta_L) - N_R \sin(\varphi - \delta_R) - mg\varphi_{SE} \qquad [3.15]$$

Vertical Equation

The derivation of the vertical equation of motion is similar to that for the lateral equation. The vertical equation is obtained by equating the acceleration in the b_2 direction to the sum of the forces in the b_2 direction. Using equations 3.12 and 3.14, the vertical equation is:

$$-m(\ddot{x} - \frac{V^2}{R})\varphi_{SE} = F_{LA_L}\sin(\varphi + \delta_L) + F_{LA_R}\sin(\varphi - \delta_R) + N_L \cos(\varphi + \delta_L) + N_R \cos(\varphi - \delta_R) - mg \qquad [3.16]$$

Yaw Equation

The yaw equation is found by using Euler's equations of motion. These equations state that the sum of the moments acting on a rigid body is equal to the time rate of change of the angular momentum vector. This law is expressed below:

$$\Sigma \underline{M} = \dot{\underline{H}} \qquad [3.17]$$

where,

$\Sigma \underline{M}$ = sum of the moment vectors

$\underline{H}$ = time rate of change of the momentum vector

The angular momentum is given by (Meirovitch, 1970):

$$\underline{H} = \underline{\underline{I}} \cdot \underline{\omega} \qquad [3.18]$$

where,

$\underline{\underline{I}}$ = inertia tensor

$\underline{\omega}$ = angular velocity vector

The time rate of change of the angular momentum is found by using the Transport theorem, equation 3.9:

$$\dot{\underline{H}} = {}^{N}\frac{d}{dt}\underline{H} = \underline{\underline{I}} \cdot {}^{R}\frac{d}{dt}\underline{\omega} + \underline{\omega} \times \underline{\underline{I}} \cdot \underline{\omega} \qquad [3.19]$$

where ${}^{R}\frac{d}{dt}$ denotes differentiation with respect to the rotating reference frame axes.

If the inertia tensor is computed with respect to the principal axes, then the products of inertia vanish. The result is that the inertia tensor is diagonal. The wheelset axes {b} correspond to the wheelset principal axes.

The wheelset angular velocity vector is defined as follows. The wheelset spins about the b_1 axis with an angular velocity of $\Omega + \dot{\beta}$. The angular velocity $\underline{\omega}^B$ for the {b} coordinate system was defined in Section 3.1. Then the wheelset angular velocity is given by:

$$\underline{\omega} = (\Omega + \dot{\beta})\hat{\underline{b}}_1 + \underline{\omega}^B = (\Omega + \dot{\beta})\hat{\underline{b}}_1 + \dot{\varphi}\hat{\underline{b}}_3 + \dot{\theta}\,\hat{\underline{c}}_2 - \frac{V}{R}\hat{\underline{a}}_2 \qquad [3.20]$$

Using the transformations given by equations 3.1 and 3.5, the angular velocity can be written in terms of the {b} coordinate system. Assuming small angles, the result is:

$$\underline{\omega} = [\Omega + \dot{\beta}]\hat{\underline{b}}_1 + \left[-\frac{V}{R} + \dot{\theta} \right]\hat{\underline{b}}_2 + \dot{\varphi}\hat{\underline{b}}_3 \qquad [3.21]$$

The time derivative of $\underline{\omega}^B$ is given by:

$$^B\frac{d}{dt}\underline{\omega} = \ddot{\beta}\hat{\underline{b}}_1 + \ddot{\theta}\,\hat{\underline{b}}_2 + \ddot{\varphi}\hat{\underline{b}}_3 \qquad [3.22]$$

Substituting equations 3.21-3.22 into equation 3.19 yields an expression for the time rate of change of the angular momentum. This expression is simplified by the symmetry of the wheelset ($I_2 = I_3$), and by ignoring small gyroscopic terms. Then $\underline{H}$ can be written as:

$$\dot{\underline{H}} = I_1\ddot{\beta}\,\hat{\underline{b}}_1 + I_2\ddot{\theta}\,\hat{\underline{b}}_2 + I_3\ddot{\varphi}\,\hat{\underline{b}}_3 \qquad [3.23]$$

This expression can be transformed to the track axes using equation 3.6. Assuming small angles:

$$\dot{\underline{H}} = I_1\ddot{\beta}\hat{\underline{b}}_1 + I_2\ddot{\theta}\,\hat{\underline{t}}_2 + I_3\ddot{\varphi}\hat{\underline{t}}_3 \qquad [3.24]$$

Next, the moment vector about the wheelset centroid is defined. The forces acting on the wheelset are given in equation 3.14. Also, referring to Figure 11, the creep spin moments $\underline{M}_{SP_{L,R}}$ must be considered. These are transformed to the track axes using equation 3.7. Then the moment vector $\Sigma\underline{M}$ can be written:

$$\begin{aligned}\Sigma\underline{M} = [\ & -M_{SP_L}\sin(\varphi + \delta_L) - M_{SP_R}\sin(\varphi - \delta_R) \\ & - F_{LO_L}r_L - F_{LO_R}r_R]\hat{t}_1 \\ & + [M_{SP_L}\cos(\varphi + \delta_L) + M_{SP_R}\cos(\varphi - \delta_R) + a(F_{LO_R} - F_{LO_L})]\hat{t}_2 \\ & + [(F_{LA_L}\cos(\varphi + \delta_L) - N_L\sin(\varphi + \delta_L))r_L \\ & + (F_{LA_R}\cos(\varphi - \delta_R) - N_R\sin(\varphi - \delta_R))r_R \\ & + (F_{LA_L}\sin(\varphi + \delta_L) + N_L\cos(\varphi + \delta_L))a \\ & - (F_{LA_R}\sin(\varphi - \delta_R) + N_R\cos(\varphi - \delta_R))a]\hat{t}_3\end{aligned} \qquad [3.25]$$

where a is the rail semi-gage length (see Figure 11).

The yaw equation is obtained from Euler's equations. The time rate of change of angular momentum in the t_2 direction is equal to the sum of the moments about the t_2 axis:

$$I_2\ddot{\theta} = (-F_{LO_L} + F_{LO_R})a + M_{SP_L}\cos(\varphi + \delta_L) + M_{SP_R}\cos(\varphi - \delta_R) \qquad [3.26]$$

Roll Equation

The derivation of the roll equation of motion is similar to that for the yaw equation. From Euler's equation, the time rate of change of the angular momentum in the t_3 direction is equal to the sum of the moments about the t_3 axis. Using equations 3.24 and 3.25, the roll equation is:

$$
\begin{aligned}
I_3\ddot{\varphi} = &(F_{LA_L}\cos(\varphi + \delta_L) - N_L \sin(\varphi + \delta_L))r_L \\
&+ (F_{LA_R}\cos(\varphi - \delta_R) - N_R \sin(\varphi - \delta_R))r_R \\
&+ (F_{LA_L}\sin(\varphi + \delta_L) + N_L \cos(\varphi + \delta_L))a \\
&- (F_{LA_R}\sin(\varphi - \delta_R) + N_R \cos(\varphi - \delta_R))a
\end{aligned}
\qquad [3.27]
$$

Spin Equation

The derivation of the spin equation of motion is similar to that for the yaw equation. From Euler's equation, the time rate of change of the angular momentum in the t_1 direction is equal to the sum of the moments about the t_1 axis. Using equations 3.24 and 3.25, the spin equation is:

$$
\begin{aligned}
I_1\ddot{\beta} = &M_{SP_L}\sin(\varphi + \delta_L) + M_{SP_R}\sin(\varphi - \delta_R) \\
&+ F_{LO_L}r_L + F_{LO_R}r_R
\end{aligned}
\qquad [3.28]
$$

3.3 Two-Point Contact

The free-body diagram of the wheelset negotiating a curve with two-point contact is shown in Figure 12. The curve is a right hand curve and thus flange contact occurs at the left wheel. A set of axes is defined at each of the two contact points on the left wheel. The reference frames $\{e_F\}$ and $\{e_T\}$ denote the contact patch axes for the flange and tread, respectively. These frames are rotated from the $\{t\}$ frame as shown below:

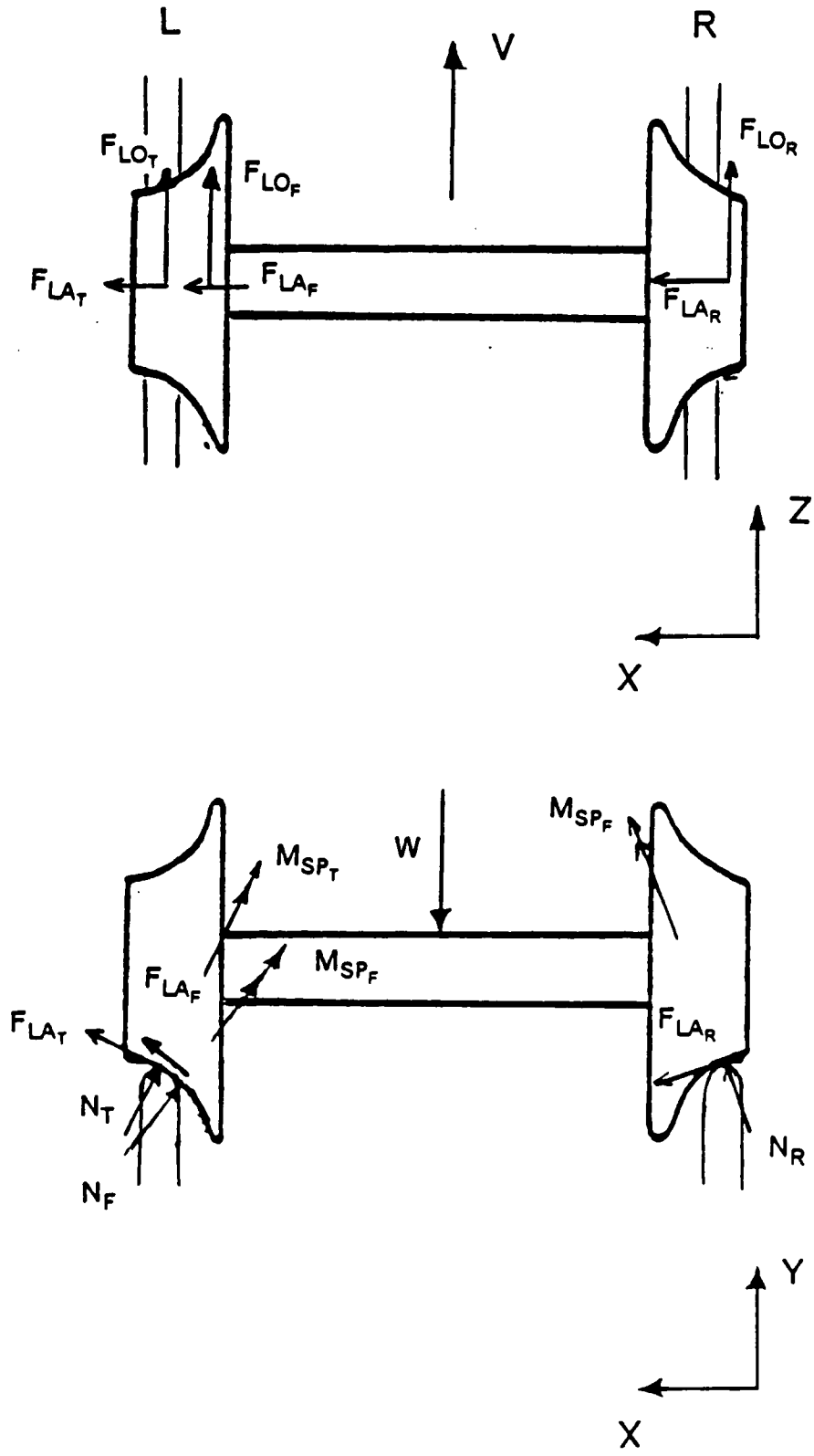

Figure 12. Free-Body Diagram for a Wheelset with Two-Point Contact

$$\{e_F\} = [R_3(\varphi + \delta_F)]\,\{t\} \qquad [3.29a]$$

$$\{e_T\} = [R_3(\varphi + \delta_T)]\,\{t\} \qquad [3.29b]$$

The angles δ_F and δ_T are the contact angles at the flange and tread, respectively.

As in the case of single-point wheel/rail contact, the creep forces are denoted by F_{LA}, F_{LO} , and M_{SP}. Two normal forces develop at the left wheel in two-point contact: N_T is the normal force at the tread and N_F is the normal force at the flange. The normal force developed at the right wheel is N_R. The three normal forces are treated as unknowns in the analysis.

When the wheel flange contacts the rail head, the wheelset lateral motion is stopped. In this state of motion, the lateral displacement is a constrained variable: $x = x_F$, where x_F is the lateral displacement to reach flange contact. The additional normal force at the flange becomes the fifth unknown in this problem.

Thus, there are five unknowns that are solved: the yaw angle, θ; the normal forces N_T, N_F , and N_R; and the steady-state change in the spin angular velocity, β. As in the case of single-point contact, five equations are written to solve for the unknowns. In the following, these equations are derived.

Lateral Equation

The position vector of the wheelset center of mass is constant in the {a} frame. Assuming $x_F << R$,

$$\underline{r} = R\hat{\underline{a}}_1 \qquad [3.30]$$

The acceleration relative to the inertial reference frame is obtained by differentiating equation 3.30 twice. Using the Transport theorem, equation 3.9, the acceleration vector is:

$$\ddot{\underline{r}} = -\frac{V^2}{R}\hat{\underline{a}}_1 \qquad [3.31]$$

This result is transformed to the {t} frame using equation 3.1:

$$\ddot{\underline{r}} = -\frac{V^2}{R}\hat{\underline{t}}_1 + \frac{V^2}{R}\varphi_{SE}\hat{\underline{t}}_2 \qquad [3.32]$$

The forces acting on the wheelset are shown in Figure 12. These forces are expressed in the contact patch reference frame:

$$\begin{aligned}
&\text{Left Tread} && \underline{F}_T = F_{LA_T}\hat{\underline{e}}_{1_T} + N_T\hat{\underline{e}}_{2_T} + F_{LO_T}\hat{\underline{e}}_{3_T} \\
&\text{Left Flange} && \underline{F}_F = F_{LA_F}\hat{\underline{e}}_{1_F} + N_F\hat{\underline{e}}_{2_F} + F_{LO_F}\hat{\underline{e}}_{3_F} \\
&\text{Right Wheel} && \underline{F}_R = F_{LA_R}\hat{\underline{e}}_{1_R} + N_R\hat{\underline{e}}_{2_R} + F_{LO_R}\hat{\underline{e}}_{3_R}
\end{aligned} \qquad [3.33]$$

These force vectors are transformed to the track axes {t} using equations 3.7 and 3.30. The resulting force vectors are:

$$\begin{aligned}
\underline{F}_T = &\left[F_{LA_T}\cos(\varphi + \delta_T) - N_T\sin(\varphi + \delta_T)\right]\hat{\underline{t}}_1 + \\
&\left[N_T\cos(\varphi + \delta_T) + F_{LA_T}\sin(\varphi + \delta_T)\right]\hat{\underline{t}}_2 + F_{LO_T}\hat{\underline{t}}_3
\end{aligned} \qquad [3.34a]$$

$$\begin{aligned}
\underline{F}_F = &\left[F_{LA_F}\cos(\varphi + \delta_F) - N_F\sin(\varphi + \delta_F)\right]\hat{\underline{t}}_1 + \\
&\left[N_F\cos(\varphi + \delta_F) + F_{LA_F}\sin(\varphi + \delta_F)\right]\hat{\underline{t}}_2 + F_{LO_F}\hat{\underline{t}}_3
\end{aligned} \qquad [3.34b]$$

$$\underline{F}_R = \left[F_{LA_R}\cos(\varphi - \delta_R) - N_R \sin(\varphi - \delta_R)\right]\hat{t}_1 + \left[N_R \cos(\varphi - \delta_R) + F_{LA_R}\sin(\varphi - \delta_R)\right]\hat{t}_2 + F_{LO_R}\hat{t}_3 \qquad [3.34c]$$

The lateral equation of motion is obtained by equating the acceleration in the t_1 direction to the sum of the forces in that direction. Using equations 3.13c, 3.32 and 3.34:

$$-m\frac{V^2}{R} = F_{LA_T}\cos(\varphi + \delta_T) + F_{LA_F}\cos(\varphi + \delta_F) + F_{LA_R}\cos(\varphi - \delta_R) - N_T \sin(\varphi + \delta_T) - N_F \sin(\varphi + \delta_F) - N_R \sin(\varphi - \delta_R) - mg\varphi_{SE} \qquad [3.35]$$

Vertical Equation

The derivation of the vertical equation of motion is similar to that for the lateral equation. The vertical equation is obtained by equating the acceleration in the t_2 direction to the sum of the forces in the t_2 direction. Using equations 3.13c, 3.32, and 3.35:

$$m\frac{V^2}{R}\varphi_{SE} = F_{LA_T}\sin(\varphi + \delta_T) + F_{LA_F}\sin(\varphi + \delta_F) + F_{LA_R}\sin(\varphi - \delta_R) + N_T \cos(\varphi + \delta_T) + N_F \cos(\varphi + \delta_F) + N_R \cos(\varphi - \delta_R) - mg \qquad [3.36]$$

Yaw Equation

The yaw equation is found using Euler's equations, as discussed in Section 3.2. The angular momentum vector for the case of two-point wheel/rail contact is the same as for the case of single-point contact. This result is given in equation 3.24.

The moment vector $\Sigma\underline{M}$ includes contributions from the wheelset forces (equation 3.34), and the spin creep moments (see Figure 12). The moment vector is:

$$\begin{aligned}
\Sigma\underline{M} = [& - M_{SP_T}\sin(\varphi + \delta_T) - M_{SP_F}\sin(\varphi + \delta_F) - M_{SP_R}\sin(\varphi - \delta_R) \\
& - F_{LO_T}r_T - F_{LO_F}r_F - F_{LO_R}r_R]\hat{1}_1 \\
& + [M_{SP_T}\cos(\varphi + \delta_T) + M_{SP_F}\cos(\varphi + \delta_F) + M_{SP_R}\cos(\varphi - \delta_R) \\
& - (F_{LO_T} + F_{LO_F} - F_{LO_R})a]\hat{1}_2 \\
& + [F_{LA_T}r_T\cos(\varphi + \delta_T) + F_{LA_F}r_F\cos(\varphi + \delta_F) + F_{LA_R}r_R\cos(\varphi - \delta_R) \\
& - N_T r_T\sin(\varphi + \delta_T) - N_F r_F\sin(\varphi + \delta_F) - N_R r_R\sin(\varphi - \delta_R) \\
& + (F_{LA_T}\sin(\varphi + \delta_T) + F_{LA_F}\sin(\varphi + \delta_F) - F_{LA_R}\sin(\varphi - \delta_R))a \\
& + (N_T\cos(\varphi + \delta_T) + N_F\cos(\varphi + \delta_F) - N_R\cos(\varphi - \delta_R))a]\hat{1}_3
\end{aligned} \qquad [3.37]$$

Finally, the yaw equation is found by equating the time rate of change of the angular momentum in the t_2 direction to the sum of the moments about the t_2 axis. Using equations 3.24 and 3.37, the yaw equation can be written:

$$\begin{aligned}
I_2\ddot{\theta} = & - (F_{LO_T} + F_{LO_F} - F_{LO_R})a + M_{SP_T}\cos(\varphi + \delta_T) \\
& + M_{SP_F}\cos(\varphi + \delta_F) + M_{SP_R}\cos(\varphi - \delta_R)
\end{aligned} \qquad [3.38]$$

Roll Equation

The derivation of the roll equation of motion is similar to that for the yaw equation. From Euler's equation, the time rate of change of the angular momentum in the t_3 direction is equal to the sum of the moments about the t_3 axis. Using equations 3.24 and 3.37, the roll equation is:

$$
\begin{aligned}
I_3\ddot{\varphi} &= F_{LA_T} r_T \cos(\varphi + \delta_T) + F_{LA_F} r_F \cos(\varphi + \delta_F) + F_{LA_R} r_R \cos(\varphi - \delta_R) \\
&\quad - N_T r_T \sin(\varphi + \delta_T) - N_F r_F \sin(\varphi + \delta_F) - N_R r_R \sin(\varphi - \delta_R) \\
&\quad + (F_{LA_T} \sin(\varphi + \delta_T) + F_{LA_F} \sin(\varphi + \delta_F) - F_{LA_R} \sin(\varphi - \delta_R))a \\
&\quad + (N_T \cos(\varphi + \delta_T) + N_F \cos(\varphi + \delta_F) - N_R \cos(\varphi - \delta_R))a
\end{aligned}
\qquad [3.39]
$$

Spin Equation

The derivation of the spin equation of motion is similar to that for the yaw equation. From Euler's equation, the time rate of change of the angular momentum in the t_1 direction is equal to the sum of the moments about the t_1 axis. Using equations 3.24 and 3.37, the spin equation is:

$$
\begin{aligned}
I_1\ddot{\beta} &= M_{SP_T} \sin(\varphi + \delta_T) + M_{SP_F} \sin(\varphi + \delta_F) + M_{SP_R} \sin(\varphi - \delta_R) \\
&\quad + F_{LO_T} r_T + F_{LO_F} r_F + F_{LO_R} r_R
\end{aligned}
\qquad [3.40]
$$

3.4 Steady-State Equations of Motion

The assumption for steady-state analysis is that the time-varying terms of the governing differential equations vanish. The resulting equations are a system of nonlinear, algebraic equations. In the following, the steady-state equations for single-point and two-point contact are obtained. The equations of motion derived in Sections 3.2 and 3.3 are used, and it is assumed that all the time-varying terms are zero.

3.4.1 Single-Point Contact

The differential equations of motion for single-point contact are derived in Section 3.2. The steady-state equations are summarized below.

Lateral Equation

$$\begin{aligned} 0 = {} & F_{LA_L}\cos(\varphi + \delta_L) + F_{LA_R}\cos(\varphi - \delta_R) \\ & - N_L \sin(\varphi + \delta_L) - N_R \sin(\varphi - \delta_R) + mg\varphi_D \end{aligned} \qquad [3.41]$$

Vertical Equation

$$\begin{aligned} 0 = {} & F_{LA_L}\sin(\varphi + \delta_L) + F_{LA_R}\sin(\varphi - \delta_R) \\ & + N_L \cos(\varphi + \delta_L) + N_R \cos(\varphi - \delta_R) \\ & - m\left(\frac{V^2}{R}\varphi_{SE} + g\right) \end{aligned} \qquad [3.42]$$

Yaw Equation

$$0 = (- F_{LO_L} + F_{LO_R})a + M_{SP_L}\cos(\varphi + \delta_L) + M_{SP_R}\cos(\varphi - \delta_R) \qquad [3.43]$$

Roll Equation

$$\begin{aligned} 0 = {} & (F_{LA_L}\cos(\varphi + \delta_L) - N_L \sin(\varphi + \delta_L))r_L \\ & + (F_{LA_R}\cos(\varphi - \delta_R) - N_R \sin(\varphi - \delta_R))r_R \\ & + (F_{LA_L}\sin(\varphi + \delta_L) + N_L \cos(\varphi + \delta_L))a \\ & - (F_{LA_R}\sin(\varphi - \delta_R) + N_R \cos(\varphi - \delta_R))a \end{aligned} \qquad [3.44]$$

Spin Equation

$$0 = M_{SP_L} \sin(\varphi + \delta_L) + M_{SP_R} \sin(\varphi - \delta_R) + F_{LO_L} r_L + F_{LO_R} r_R \qquad [3.45]$$

The term φ_D in the lateral equation is the cant deficiency:

$$\varphi_D = \frac{V^2}{Rg} - \varphi_{SE} \qquad [3.46]$$

The cant deficiency is an angular measure of the lateral force imbalance between the centrifugal and gravitational forces.

3.4.2 Two-Point Contact

The differential equations of motion for two-point contact are derived in Section 3.3. The steady-state equations are summarized below.

Lateral Equation

$$0 = F_{LA_T} \cos(\varphi + \delta_T) + F_{LA_F} \cos(\varphi + \delta_F) + F_{LA_R} \cos(\varphi - \delta_R) - N_T \sin(\varphi + \delta_T) - N_F \sin(\varphi + \delta_F) - N_R \sin(\varphi - \delta_R) + mg\varphi_D \qquad [3.47]$$

Vertical Equation

$$0 = F_{LA_T}\sin(\varphi + \delta_T) + F_{LA_F}\sin(\varphi + \delta_F) + F_{LA_R}\sin(\varphi - \delta_R) + N_T\cos(\varphi + \delta_T) + N_F\cos(\varphi + \delta_F) + N_R\cos(\varphi - \delta_R) - m\left(\frac{V^2}{R}\varphi_{SE} + g\right) \quad [3.48]$$

Yaw Equation

$$0 = -(F_{LO_T} + F_{LO_F} - F_{LO_R})a + M_{SP_T}\cos(\varphi + \delta_T) + M_{SP_F}\cos(\varphi + \delta_F) + M_{SP_R}\cos(\varphi - \delta_R) \quad [3.49]$$

Roll Equation

$$0 = F_{LA_T}r_T\cos(\varphi + \delta_T) + F_{LA_F}r_F\cos(\varphi + \delta_F) + F_{LA_R}r_R\cos(\varphi - \delta_R) - N_Tr_T\sin(\varphi + \delta_T) - N_Fr_F\sin(\varphi + \delta_F) - N_Rr_R\sin(\varphi - \delta_R) + (F_{LA_T}\sin(\varphi + \delta_T) + F_{LA_F}\sin(\varphi + \delta_F) - F_{LA_R}\sin(\varphi - \delta_R))a + (N_T\cos(\varphi + \delta_T) + N_F\cos(\varphi + \delta_F) - N_R\cos(\varphi - \delta_R))a \quad [3.50]$$

Spin Equation

$$0 = M_{SP_T}\sin(\varphi + \delta_T) + M_{SP_F}\sin(\varphi + \delta_F) + M_{SP_R}\sin(\varphi - \delta_R) + F_{LO_T}r_T + F_{LO_F}r_F + F_{LO_R}r_R \quad [3.51]$$

3.5 Summary

This chapter shows the derivation of the equations of motion for a wheelset on curved track. The equations include both single-point and two-point wheel/rail contact conditions. The generalized forces in the equations of motion are the wheel/rail contact forces. In the next chapter, the finite element method is discussed as a method to calculate these contact forces.

The wheelset steady-state equations were obtained by dropping the time-varying terms from the differential equations of motion. The steady-state equations constitute a system of nonlinear, algebraic equations. Newton's method is used to solve these equations in Chapter 5.

Chapter 4

Finite Element Analysis of the Contact Mechanics Problem

The basic principles of mechanics of a wheelset traversing a curved track were presented in the last two chapters. The wheel/rail contact problem and the resulting creep forces were discussed in Chapter 2. These creep forces were used to develop the equations of motion of a wheelset on curved track in Chapter 3. A solution to this twofold problem is presented in the following chapters. In this chapter, a method is presented for computing the rolling contact forces using the finite element method. In Chapter 5, a method is presented for solving the nonlinear equations of motion.

The ABAQUS finite element program (ABAQUS User's Manual, 1985) was used unsuccessfully as a method to calculate the wheel/rail creep forces. ABAQUS is a nonlinear finite element program which is capable of solving the contact problem as discussed in Section 2.3. The model used to represent the wheel, rail, and wheel/rail interface is presented in this chapter. Also, the method used to simulate the wheel

rolling with creep is discussed. The pre- and post-processing programs used in this analysis are briefly outlined. Finally, several example contact problems and rolling contact problems are presented.

4.1 Finite Element Model

Generally, there are four characteristics which describe a finite element model:

- model geometry
- element type
- material properties
- boundary conditions

The first three characteristics are discussed below for the wheel/rail finite element model. The boundary conditions for the model are discussed in the following section.

The wheel and rail structures are shown in Figure 13a. Recall from Section 2.1 that only a small part of the wheel and rail are deformed near the region of contact. The remainder of these bodies undergo rigid-body displacements. This fact was used to simplify the wheel/rail model. Only a relatively small portion of the wheel and rail near the region of contact was modelled.

This simplification is justified in two ways. First, the parts of the wheel and rail which are not modelled are undergoing approximately rigid-body motion. This motion can be accounted for by the boundary conditions alone. Second, all the information required by the analysis is still present in the simplified model. The contact patch geometry, stress distribution, and reaction forces can be solved accurately.

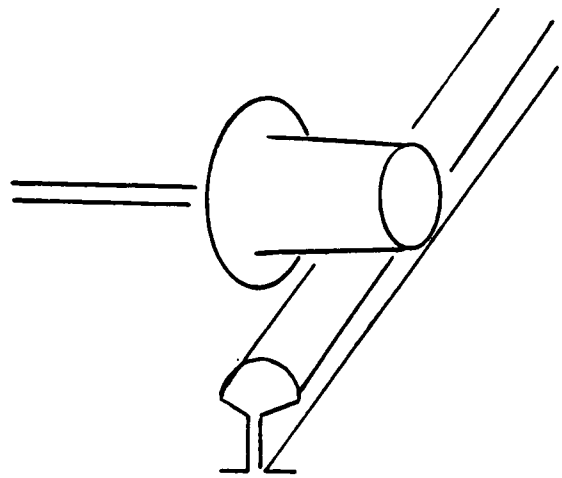

a) Wheel and Rail Structures

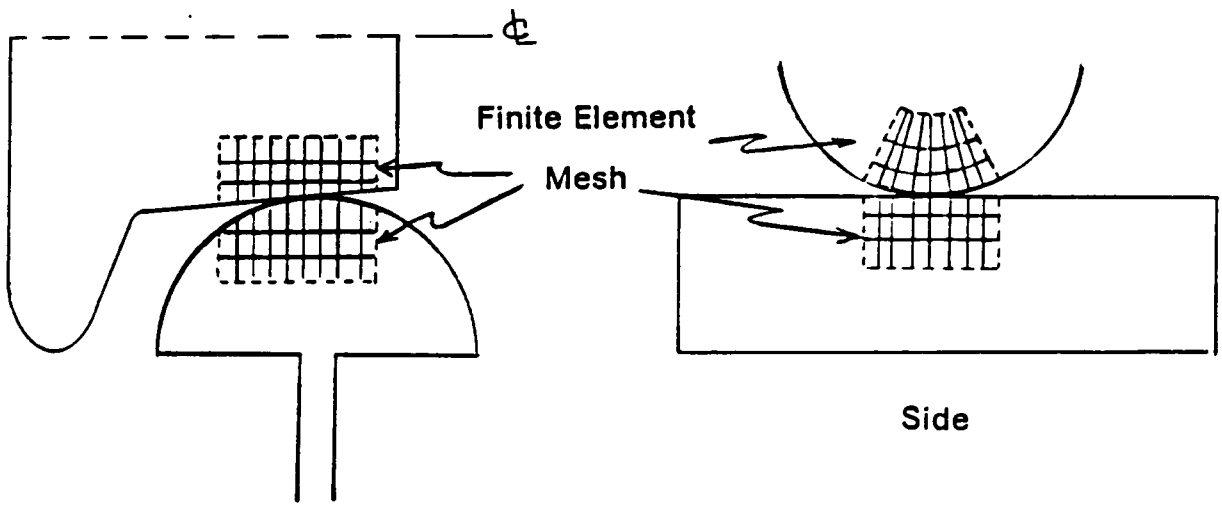

b) Finite Element Discretization

Figure 13. Wheel/Rail Finite Element Model Geometry

A typical model geometry is shown in Figure 13b. The wheel geometry is obtained by revolving the wheel profile around the wheel's axis of revolution. The wheel profile is usually specified by a set of equations or by a set of coordinates. The rail head geometry is obtained by extruding the rail head profile through some distance. The rail head profile is also specified using equations or coordinates.

The wheel and rail were modelled using isoparametric, parabolic, solid elements. Two such elements were used (see Figure 14): a 20-node element and a 27-node variable node element. The 27-node variable node element was used in the layer of elements adjacent to the contact surface. This element allowed the use of an extra node on the contact surface. Thus better accuracy was obtained in the contact analysis. The 20-node element was used in the remainder of the model. This modelling technique is recommended by HKS (ABAQUS User's Manual, 1985). Geometric nonlinearities were not included in the analysis.

The wheel/rail interface was modelled using an 18-node interface element, shown in Figure 15. This element connects corresponding nodes on the wheel and rail bodies. The interface element detects contact between the two bodies. The element transmits the normal and shear contact forces when a contact condition exists.

The solid elements are isotropic and linearly elastic. These elements are characterized by the elasticity constants: Youngs modulus, E, and Poisson's ratio, ν . The properties of steel were used for both the wheel and the rail:

$$E = 30 \times 10^6 \quad \text{psi}$$

$$\nu = 0.30$$

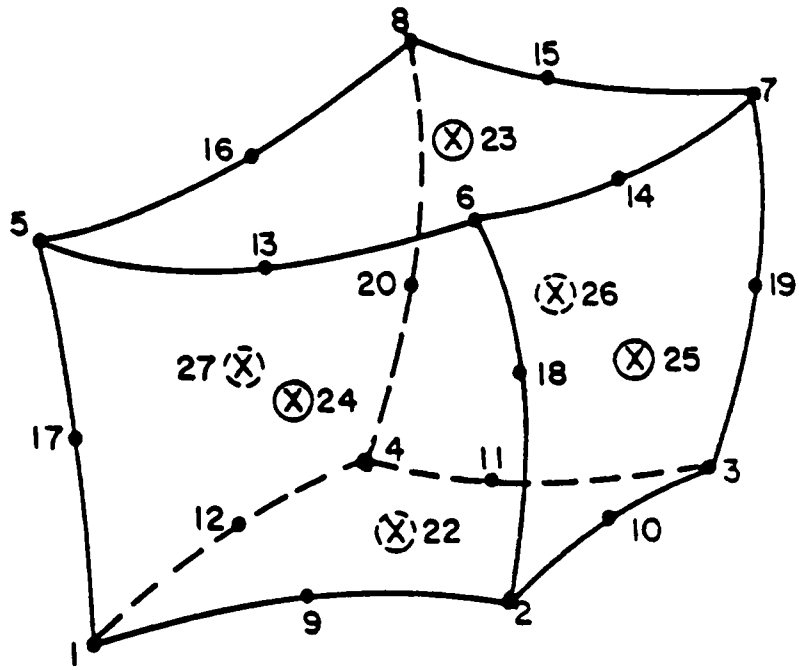

27-Node Element

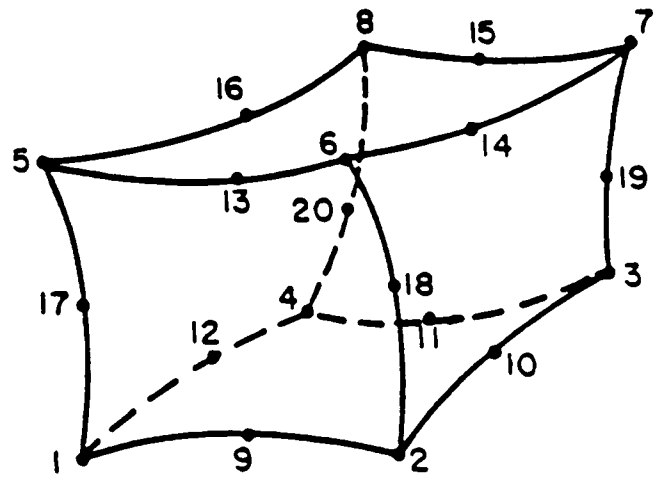

20-Node Element

Figure 14. 3-D Continuum Elements Used to Model Wheel and Rail (ABAQUS User's Manual, 1985)

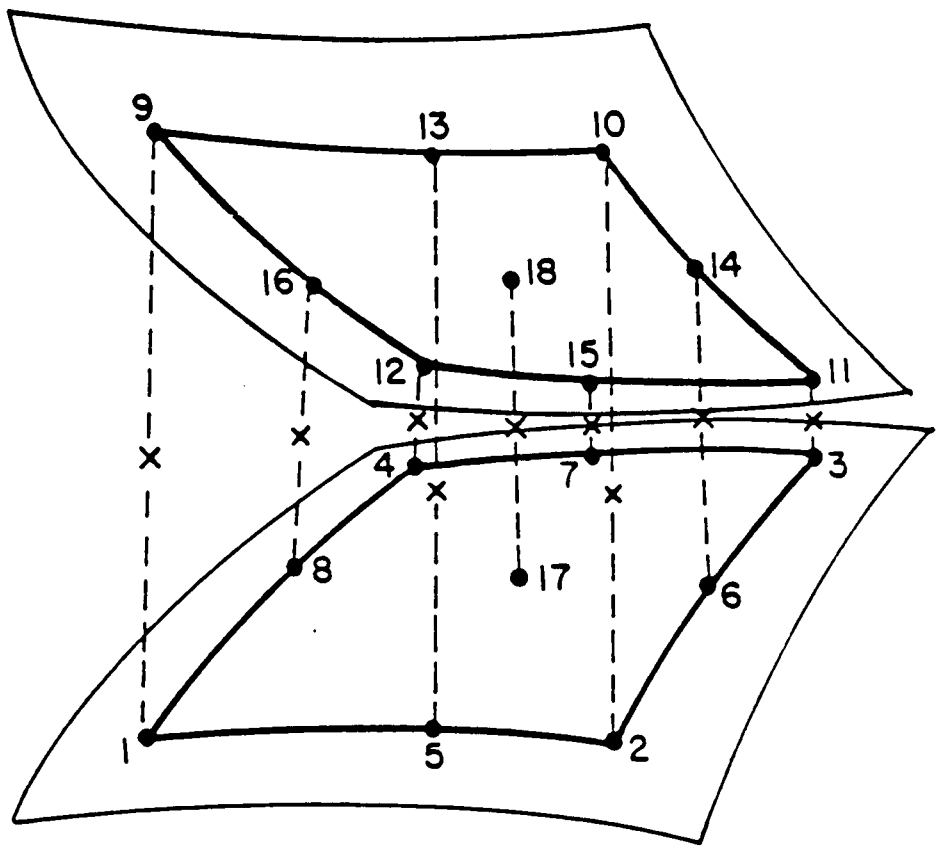

Figure 15. Interface Element Used to Model Contact Surface (ABAQUS User's Manual, 1985)

The interface elements obey the Coulomb friction law, with the addition of the stiffness-in-stick coefficient discussed in Chapter 2. The Coulomb friction law is characterized by the coefficient of friction, μ. The value of μ depends on the "cleanliness" of the contacting surfaces. Oily, wet, and contaminated surfaces tend to reduce μ. In the present analysis, the value of μ was:

$$\mu = 0.65$$

4.2 *Analysis of the Creep Forces*

The analysis of the creep forces was completed in two steps. First, a static load was applied to the model to simulate the weight supported on the contact patch. Second, the wheel was "rolled" on the rail with some amount of slip. The static load remained constant throughout the "rolling" step. The creep forces were obtained by summing the reaction forces on the wheel. This analysis procedure is discussed in greater detail below.

4.2.1 Static Analysis

The model configuration for the static load is shown in Figure 16. The wheel is constrained by "rollers" placed on all the interior edges. The rail is constrained in the 2- and 3-directions by "rollers" on the interior edges.

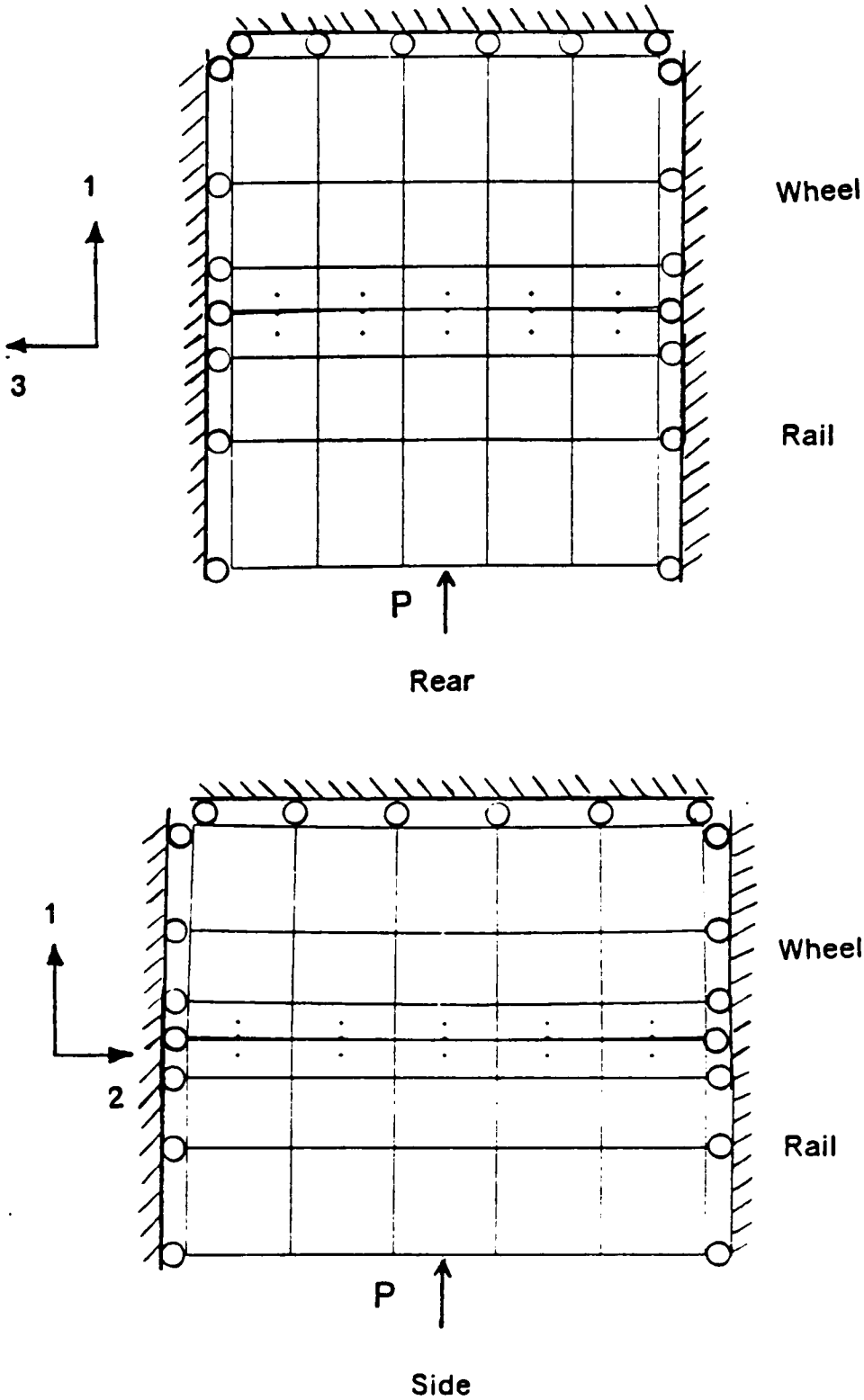

Figure 16. Model Configuration for Static Analysis

The static load is applied to the rail as follows. All nodes on the bottom edge of the rail are constrained to have the same vertical displacement. This is done by leaving one node active and reducing the remaining nodes on the edge out of the problem. Then a vertical force P is applied to the active node. This load remains in place for the subsequent rolling analysis.

The vertical load is reacted by the rollers along the top edge of the wheel. The sum of the reaction forces at these rollers is equal and opposite to the applied load. This can be written as:

$$\sum_i R_1^i = -P \qquad [4.1]$$

where R_1^i denotes the reaction force at the i'th constraint in the 1-direction.

4.2.2 Longitudinal Creep Force Analysis

In this analysis it is necessary to simulate the wheel rolling with slip, or creepage. This is done by making use of the rigid-body behavior of the wheel in the contact problem. The interior edges of the wheel model are assumed to be sufficiently far from the contact region so their displacements are rigid-body diplacements. Then the motion of these edges is kinematically constrained and can be specified exactly.

The creepage is introduced into the rolling as follows. Figure 17a shows a point Q on the wheel which undergoes rigid-body motion. In Figure 17b, the point has moved to a new position Q'. In doing so, the wheel has rotated by an amount θ and translated longitudinally by an amount y. When the wheel rolls "perfectly", with no

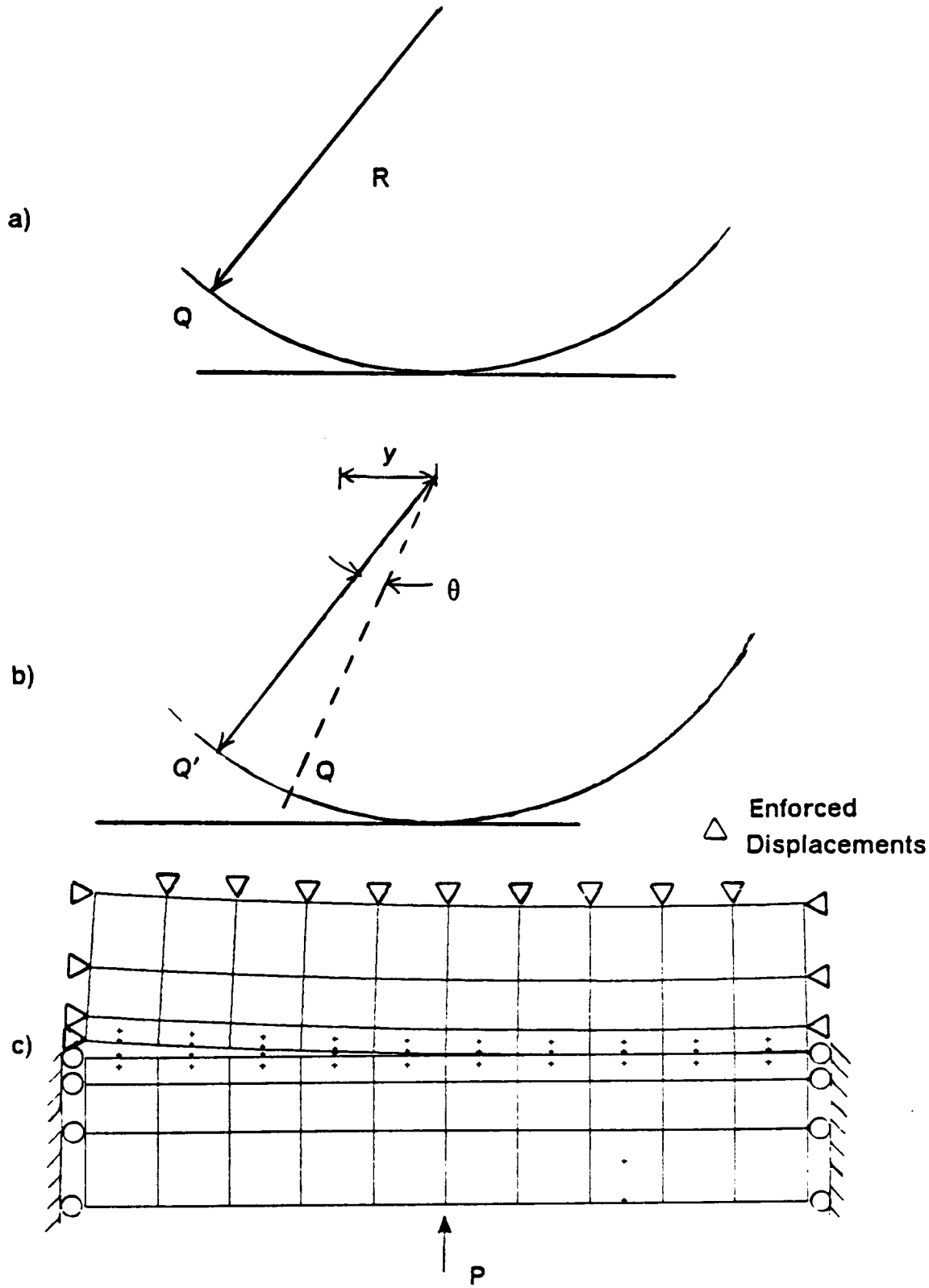

Figure 17. Boundary Conditions for Longitudinal Creepage

creepage, then $y = R\theta$. In order to introduce creepage, the wheel translation is specified such that $y \neq R\theta$.

The longitudinal creepage is defined as:

$$\zeta_{LO} = \frac{y - R\theta}{y} \qquad [4.2]$$

Thus braking ($y > R\theta$) corresponds to a positive creepage, and traction ($y < R\theta$) corresponds to a negative creepage. Given ζ_{LO} and y, the rigid-body position of the wheel is kinematically constrained. The position of the interior edges of the wheel model are determined in this manner. The new position of each node on these edges is computed and specified using enforced displacement boundary conditions. The loading configuration is shown in Figure 17c.

This method for simulating rolling changed the constraint condition on the interior edges of the model. The roller type boundary conditions were replaced by point constraints. This change was necessary to model the position of the wheel as it rolled along the rail surface. This rolling simulation could not be achieved using the roller type boundary conditions. The point constraints allowed specification of the exact location of the wheel boundary in a kinematically constrained position.

The longitudinal creep force generated by the above loading scheme is reacted by the wheel. The sum of the reaction forces at the wheel constraints is equal and opposite to the creep force:

$$\sum_i R_2^i = - F_{LO} \qquad [4.3]$$

4.3 Pre- and Post-Processing Programs

This analysis required the preparation of hundreds of finite element models. Subsequently, voluminous amounts of finite element results were reduced to obtain the creep forces. Several pre- and post-processing programs were written to facilitate the analysis. These are described below.

Finite Element Model Generation Program (FEMG)

The FEMG program is pre-processor that creates the finite element model data file. This file includes:

- nodal coordinates (model geometry)
- node set definitions
- node constraint equations
- element connectivity
- material properties

The user provides data for the wheel and rail profiles, the contact position on the wheel and rail, and for the mesh density.

Rolling Boundary Conditions Program (RBC)

The RBC program is a pre-processor that computes the boundary conditions to simulate rolling. The user supplies the distance rolled and the creepage. The program calculates the displaced position $\underline{r}'$ of the nodes on the edge of the wheel. The

superscript i denotes the i'th step in rolling. The value for the enforced displacement boundary condition is found by:

$$\Delta = r^i - r^0 \qquad [4.4]$$

where r^0 is the initial coordinate of the node. This calculation is done for the nodes on the interior boundaries of the wheel at each step i.

Reaction Force Post-Proccessor (RFPP)

The RFPP is used to determine the reaction loads on the wheel and the rail from the rolling analysis. The program scans the finite element program output file, and locates the section of output containing the boundary condition reaction forces. These forces are summed for the three directions, for both the wheel and the rail.

4.4 Example #1: Hertzian Contact Problem

The first example is a static analysis of two cylinders perpendicular to one another, shown in Figure 18a. The top and bottom cylinders are referred to as cylinder 1 and cylinder 2, respectively. The principal radii of curvature of the two cylinders are:

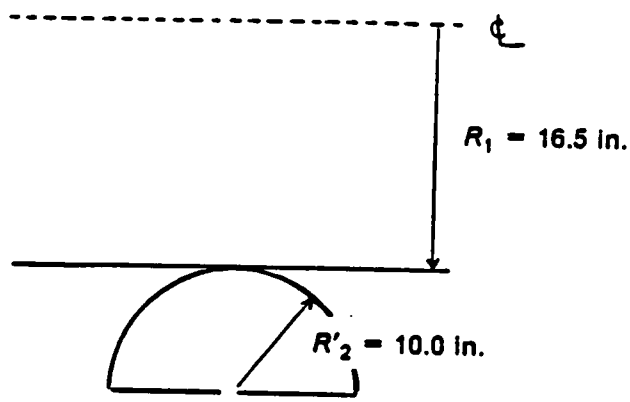

a) Two Perpendicular Cylinders

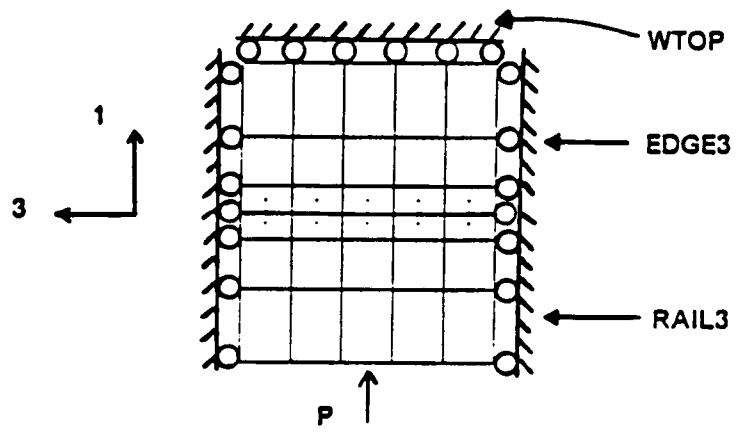

Rear

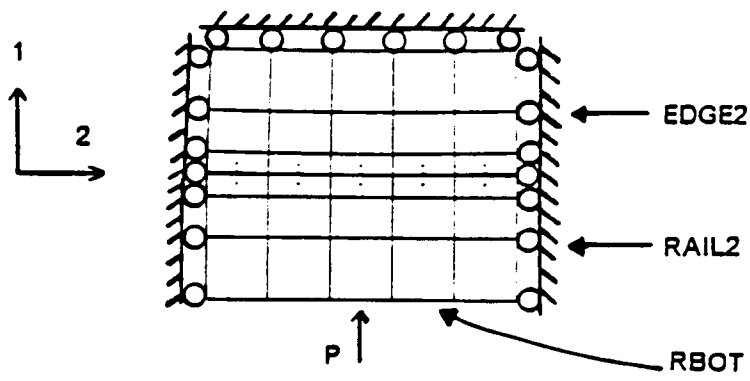

Side

b) Finite Element Model

Figure 18. Example #1: Hertzian Contact Problem

$$R_1 = 16.5 \text{ inches}$$

$$R'_1 = \infty$$

$$R_2 = \infty$$

$$R'_2 = 10.0 \text{ inches}$$

where the subscript denotes the cylinder number. The two cylinders are pressed together by a load P = 3500 pounds.

The finite element representation of the contact region is shown in Figure 18b. The model used 3618 degrees-of-freedom (DOF) and 175 parabolic elements. The interior edges were constrained by "roller" type boundary conditions. On the wheel, the node set "WTOP" was constrained in the 1-direction (see Figure 18a); the node set "EDGE2" was constrained in the 2-direction; and the node set "EDGE3" was constrained in the 3-direction. On the rail, the node set "RAIL2" was constrained in the 2-direction and the node set "RAIL3" was constrained in the 3-direction. The nodes in set "RBOT" were constrained to have the same motion in the 1-direction. One node remained active in the set. The load P was applied to this node.

The theoretical solution to this problem is obtained using the equations from Section 2.2. First, the geometry parameters A and B are computed using equation [2.2]:

$$A = \frac{1}{2}\left(\frac{1}{R_1} + \frac{1}{R_2}\right) = 0.030303 \text{ in}^{-1}$$

$$B = \frac{1}{2}\left(\frac{1}{R'_1} + \frac{1}{R'_2}\right) = 0.05 \text{ in}^{-1}$$

Next, the various stress and deflection factors are found from Figure 4. For $\frac{B}{A} = 1.65$, these are:

$$k = 0.70$$

$$c_b = 0.78$$

$$c_\sigma = 0.73$$

The semi-radii of the contact ellipse are given by equation [2.6]:

$$a = \frac{1}{k} b$$

$$b = c_b \sqrt[3]{P\Delta}$$

where

$$\Delta = \frac{1}{A + B}\left(\frac{1 - \nu_1^2}{E_1} + \frac{1 - \nu_2^2}{E_2}\right) = 7.55 \times 10^{-7} \text{ in}^3 \text{ lb}^{-1}$$

$$P = 3500 \text{ lb.}$$

Therefore, the semi-radii are:

$$a = 0.154 \text{ inches}$$

$$b = 0.108 \text{ inches}$$

The maximum normal stress at the center of the contact patch is given by equation [2.7]:

$$\sigma_{max} = c_\sigma\left(\frac{b}{\Delta}\right) = 104. \text{ ksi}$$

The normal stress distribution in the contact patch is elliptical and can be written as:

$$\sigma_1(y,z) = \sigma_{max}\left[1 - \left(\frac{y}{a}\right)^2 - \left(\frac{z}{b}\right)^2\right]^{\frac{1}{2}}$$

The theoretical and finite element results are compared in Figure 19. The finite element results agree well with the Hertz solution at the computed locations.

4.5 Example #2: Non-Hertzian Contact Problem

The second example is a static analysis of two axisymmetric bodies perpendicular to one another, shown in Figure 20a. Body 1 has a discontinuous radius of curvature R'_1 at the point of contact, $z = 0$:

$$R_1 = 16.5 \text{ inches}$$
$$R'_1 = \infty \qquad z < 0$$
$$R'_1 = 14.0 \text{ inches} \qquad z > 0$$

Body 2 is cylindrical and has the same dimensions as in Example #1:

$$R_2 = \infty$$
$$R'_2 = 10.0 \text{ inches}$$

The two bodies are pressed together by a force $P = 3500$ pounds.

The finite element representation of the contact region is shown in Figure 20b. The model is comprised of 3618 DOF and 175 parabolic elements. The boundary conditions are the same as for the model in Example #1.

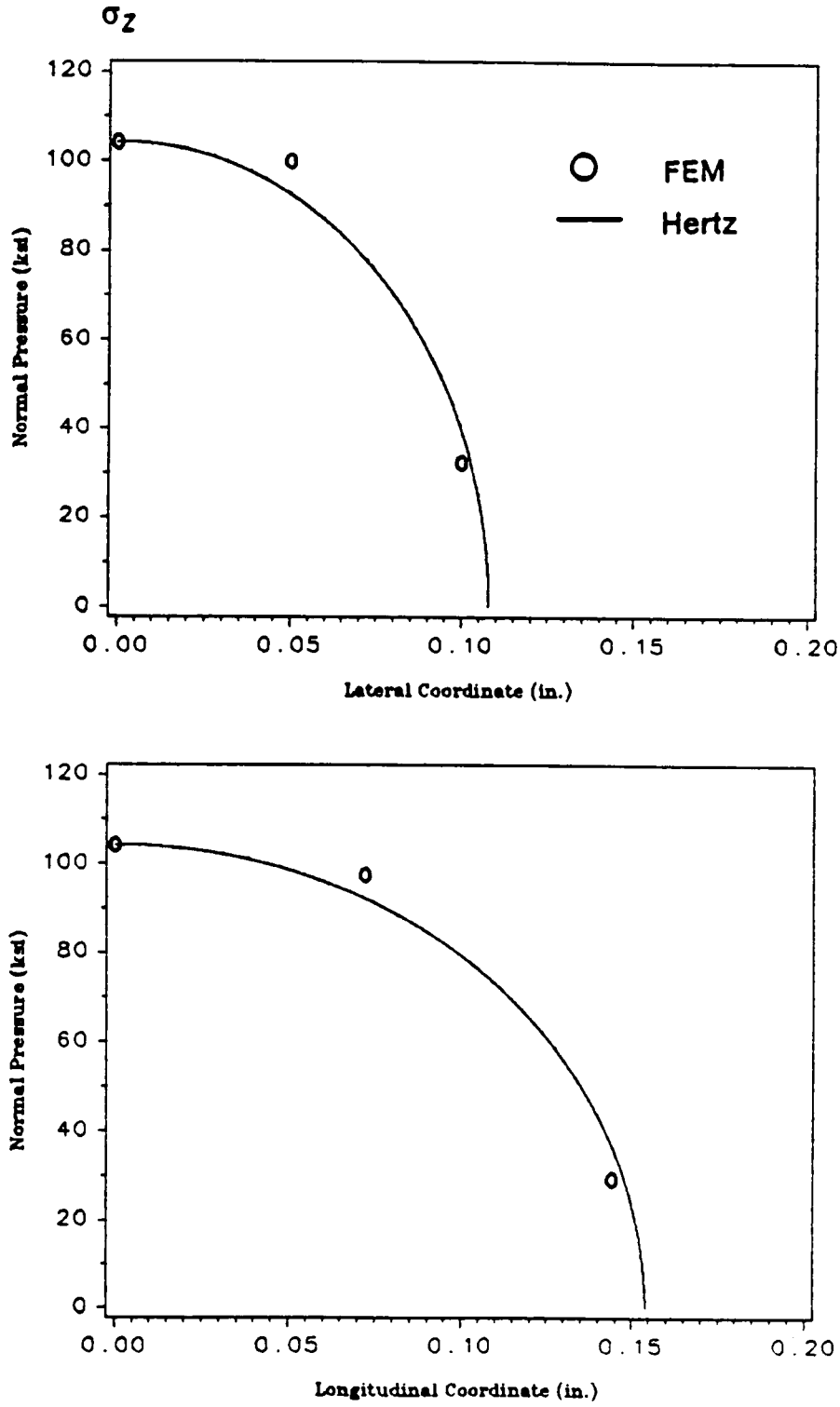

Figure 19. Comparison of Theoretical and FEM Results for Hertzian Contact Problem

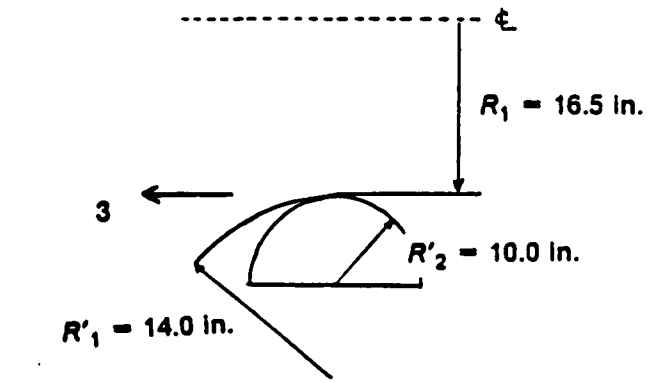

a) Two Perpendicular Axisymmetric Bodies

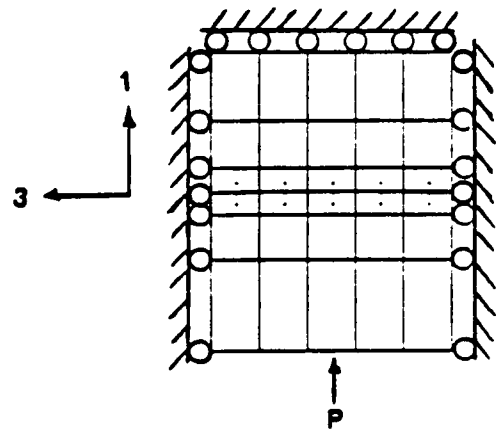

Rear

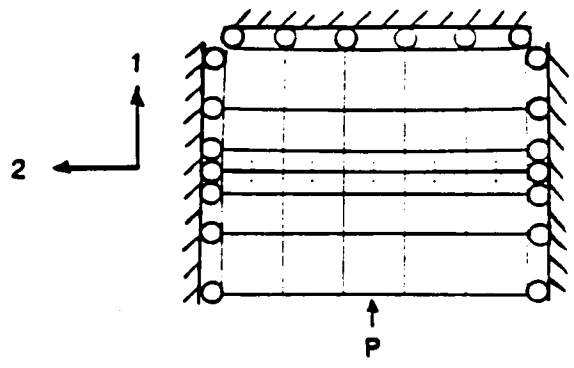

Side

b) Finite Element Model

Figure 20. Example #2: Non-Hertzian Contact Problem

The theoretical solution for this non-Hertzian contact problem is not available in closed form. However, a numerical solution to the problem was obtained using the computer program CONWHEEL (Paul and Singh, 1982). CONWHEEL uses a finite difference method to discretize and solve the equilibium equations in the contact patch.

The CONWHEEL and finite element results are compared in Figure 21. The finite element stress results agree well with the CONWHEEL solution. The contact patch shape predicted by the finite element method also matches the CONWHEEL solution.

4.6 *Example #3: Rolling Contact Problem*

The third example is a rolling contact analysis of two cylindrical bodies perpendicular to one another. The geometry of the two cylinders is the same as for the static Hertzian contact example. The problem is shown again in Figure 22a.

The finite element representation is similar to that of Example #1. However, for this example, the length of the model in the rolling direction was increased to allow the model to roll some distance. The finite element mesh is shown in Figure 22b. The model used 6831 DOF and 350 parabolic elements.

The loading was applied in two steps. The first step applied a vertical load to the model to simulate the wheelset weight. The boundary conditions for this step were the same as for Example #1. The vertical load remained in place for the subsequent rolling analysis.

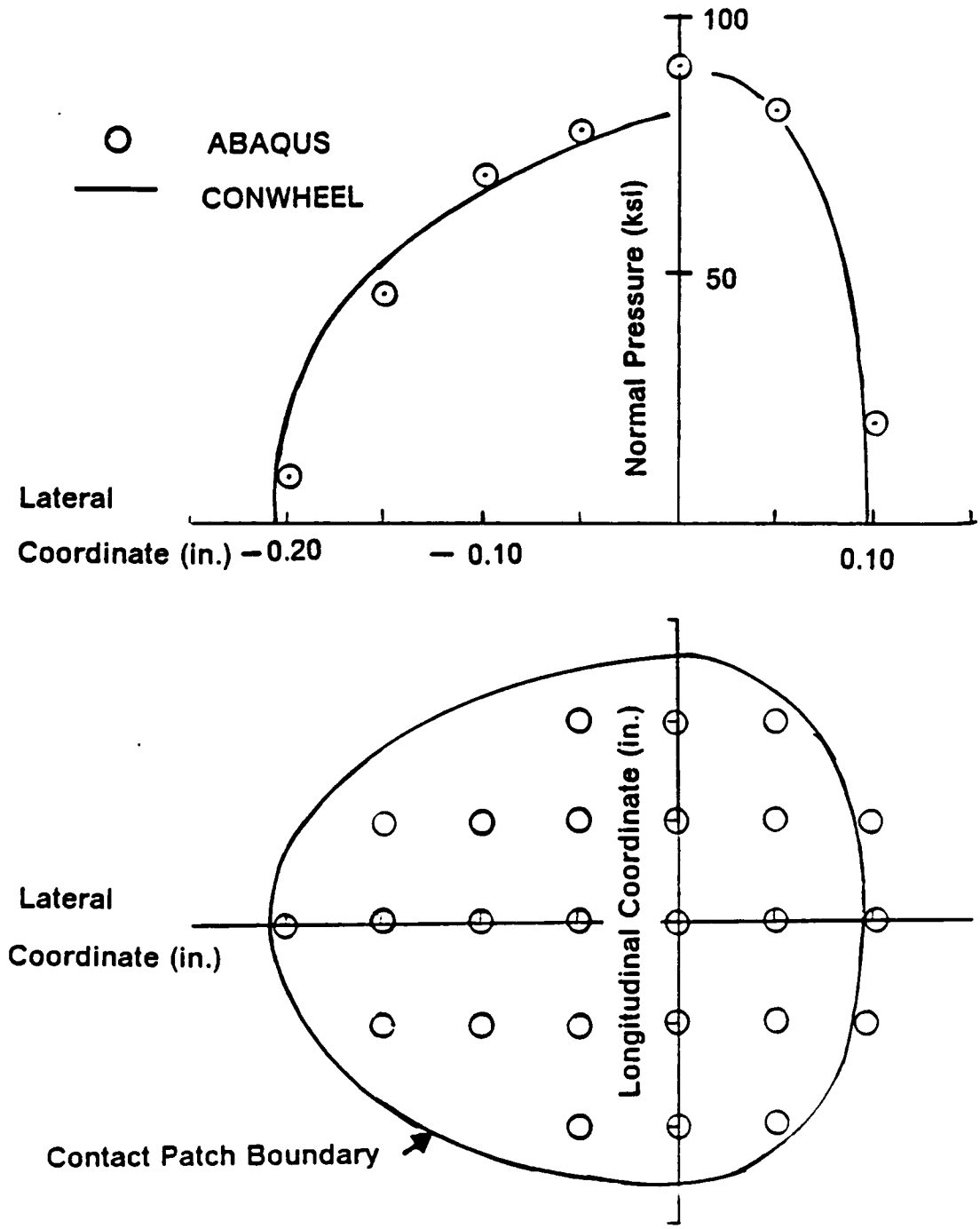

Figure 21. Comparison of CONWHEEL and FEM Results for Non-Hertzian Contact Problem

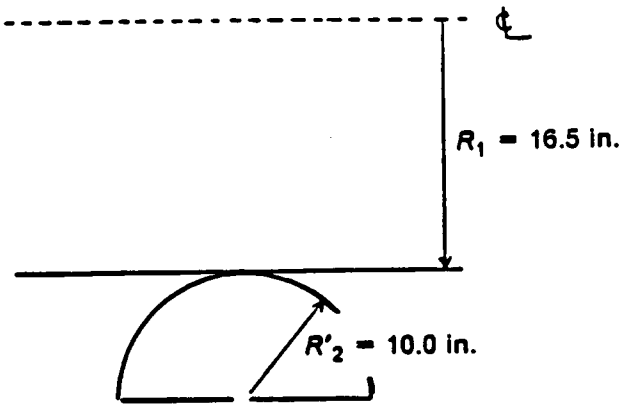

a) Two Perpendicular Cylinders

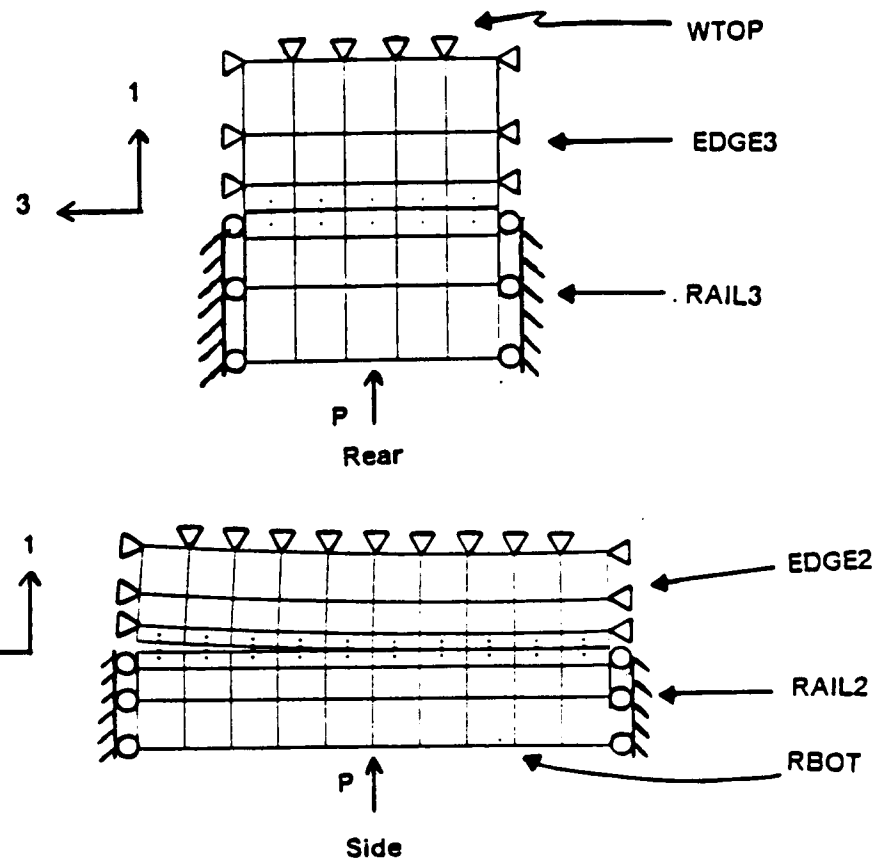

b) Finite Element Model

Figure 22. Example #3: Rolling Contact Problem

The next step was to roll the wheel along the rail. This was done by specifying the displacement of the wheel edges. These displacements were determined according to equation 4.4 to introduce a specified creepage as the wheel rolled. The boundary conditions on the rail remained constant for the rolling analysis.

The rolling step was actually completed in several substeps. In each substep of the rolling analysis the wheel was rolled by a small increment with a specified longitudinal creepage. The increment was kept small to assure convergence of the nonlinear finite element solution.

In the first example run with this model, the creepage was set to a relatively large value, $\zeta_{LO} = 0.01$. The model was run with an increment $dy = 0.05$ inches. The results for this case are shown in Figure 23. The creep force which develops reaches the adhesion limit within two steps. This is the expected result for a large creepage.

In the second example run with this model, the creepage was set to $\zeta_{LO} = 0.001$. According to Kalker's theory, this level of creepage should produce a creep force below the adhesion limit. The results for this case are shown in Figure 24. The creep force increases and reaches a steady value as the wheel rolls. However, the steady-state value is less than the creep force predicted by Kalker's theory.

Several changes were made to the model in an attempt to make the finite element results match Kalker's theory. Some of these changes had little effect. For instance, changing the translation increment did not significantly affect the results. Also, changing the method of modelling the wheelset rolling did not make a difference. In this case the rail was translated in the negative y-direction while the wheelset was

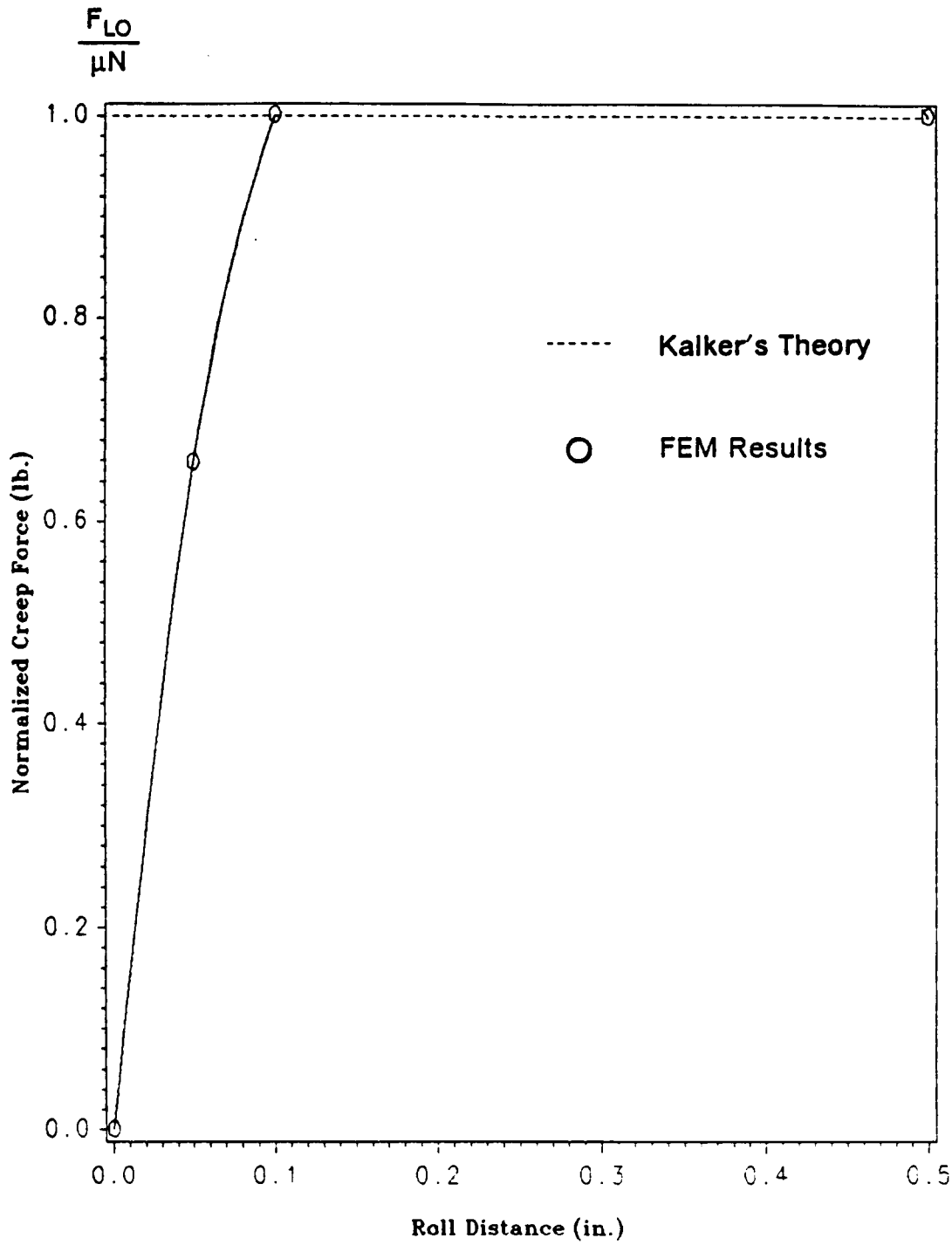

Figure 23. Creep Force Results for Rolling with Large Creepage

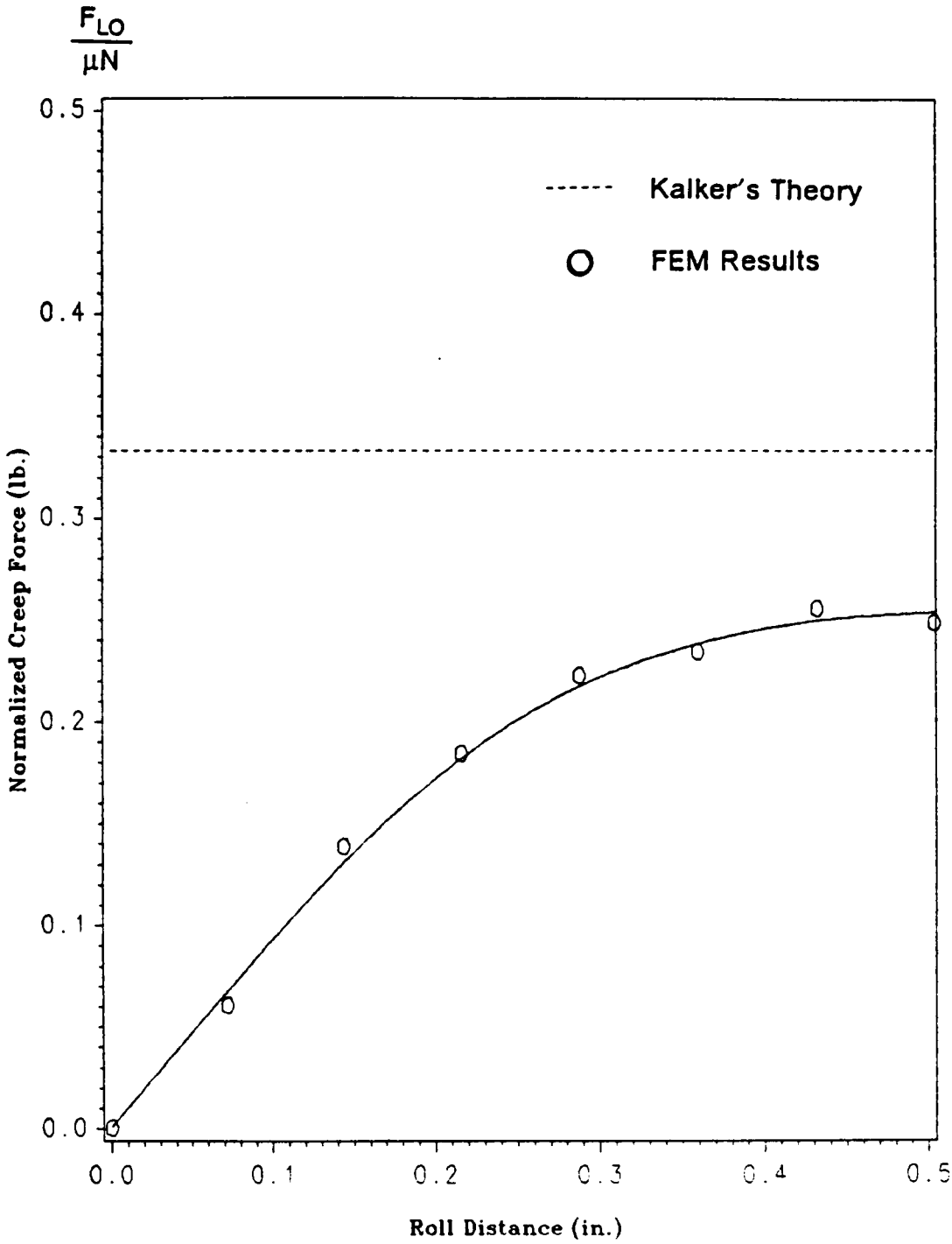

Figure 24. Creep Force Results for Rolling with Small Creepage

spun about its axis. This produced the same results as for the wheelset spining and translating.

One parameter did significantly affect the results as it was varied. This was the "stiffness-in-stick" (SIS) coefficient, a property of the interface element. The SIS transfers the shear force across the interface element when a contact condition exists. As the SIS was increased, the creep force increased. For large values of SIS the nonlinear finite element equation solver encountered numerical difficulty. The variation of the steady value of the creep force as a function of the SIS is shown in Table 1. For SIS values greater than 5×10^8, the finite element algorithm could not converge to a solution. For SIS values below 5×10^8, the creep force does not reach the value predicted by Kalker's theory.

Table 1. Normalized Creep Force versus SIS (Creepage = 0.001)

SIS	Normalized Creep Force
1.E7	0.0371
1.E8	0.2500
5.E8	no convergence

4.7 Summary

The work described in this chapter attempted to calculate the wheel/rail contact forces using the finite element method. The wheel/rail model and analysis technique were discussed. Several pre- and post-processing programs were presented. The

static contact problem was solved correctly for both Hertzian and non-Hertzian contact geometries. However, the method was not successful in solving the rolling contact problem. The rolling contact force results would have been used to solve the wheelset steady-state curving equations in the next chapter.

It appears that the major unresolved problem in the application of ABAQUS to the problem of rolling contact with slip is associated with the stiffness-in-stick parameter. When a low value of this parameter was used, the elasticity of the contact element in shear was significant in comparison to the elasticity of the contacting bodies. Therefore the stiffness-in-stick parameter influenced the results. Convergence of the nonlinear finite element code could not be achieved when a higher SIS value was used.

Chapter 5

Solution of the Steady-State Equations of Motion

The derivation of the steady-state equations of motion was included in Chapter 3. The work reported in this chapter was accomplished to provide a basis for a computer solution to the steady-state equations. This solution was to have incorporated the finite element computation of the contact forces. The solution presented in this chapter using Kalker's method was intended to be a reference solution.

The equations of motion constitute a system of five nonlinear, algebraic equations in five unknowns. Solving the system of nonlinear equations requires the use of an iterative method. Newton's method in several variables was chosen since it exhibits quadratic convergence (Johnson and Reiss, 1982). In the following, Newton's method and its implementation are discussed.

5.1 Newton's Method in Several Variables

The nonlinear equations can be written in the form:

$$f_i(x_1, x_2, \ldots, x_n) = 0 \qquad i = 1, 2, \ldots, n \qquad [5.1]$$

where the f_i are nonlinear functions, and the x_i are the unknown variables. The problem statement can be simplified by using vector notation (Johnson and Reiss, 1982). Let $\underline{x} = \{x\} = \{x_1 \;\; x_2 \;\; \ldots \;\; x_n\}^T$ be a vector containing the n solution variables. Then the system of equations in 5.1 can be written as:

$$\{F(\underline{x})\}^T = \{f_1(\underline{x}) \;\; f_2(\underline{x}) \;\; \ldots \;\; f_n(\underline{x})\} = \{0\}^T \qquad [5.2]$$

Newton's method is a fixed-point iteration sheme. The iterative method results in a series of iterates $\{x\}_{i+1}$ that converges quadratically to the solution of equation 5.1. This series is given by:

$$\{x\}_{i+1} = \{x\}_i - [J(\underline{x}_i)]^{-1}\{F(\underline{x}_i)\} \qquad [5.3]$$

where $[J(\underline{x}_i)]$ is the Jacobian of $\{F\}$ at $\underline{x}_i$.

The Jacobian matrix represents the derivative of $\{F\}$ with respect to the solution vector $\underline{x}$. That is, the (i,j)th component of the Jacobian matrix is the derivative of the i'th equation with respect to the j'th variable:

$$J_{i,j}(\underline{x}) = \frac{\partial f_i(\underline{x})}{\partial x_j} \qquad [5.4]$$

In practice, it is numerically inefficient to compute the inverse of a matrix. Thus the series in equation 5.3 is computed as follows. A new variable {dx} is defined: $\{dx\}_{i+1} = \{x\}_{i+1} - \{x\}_i$. Then equation 5.3 is rewritten as:

$$[J(\underline{x}_i)]\{dx\}_{i+1} = -\{F(\underline{x}_i)\} \qquad [5.5]$$

Equation 5.5 represents a system of simultaneous equations that can be solved by a linear equation solver. After solving for {dx}, the next iterate is found by:

$$\{x\}_{i+1} = \{x\}_i + \{dx\}_{i+1} \qquad [5.6]$$

Equations 5.5 and 5.6 are used to compute the series $\{x\}_{i+1}$ that converges to the solution of equation 5.1.

A convergence criteria is required to stop the iteration. A useful criteria is the norm of a vector. A norm is a function that gives some measure of the size of a vector. For this analysis, the infinity norm of {dx} was used. The infinity norm is equal to the largest component of a vector:

$$\|dx\|_\infty = \max\{|dx_1|, |dx_2|, \ldots, |dx_n|\} \qquad [5.7]$$

The iteration is stopped when $\|dx\|_\infty$ is less than some tolerance, δ:

$$\|dx\|_\infty < \delta \qquad [5.8]$$

Then $\{x\}_{i+1}$ is taken as the solution.

5.2 The Jacobian Matrix

The Jacobian matrix is a square matrix defined by equation 5.4. It is necessary that the Jacobian matrix be computed accurately to ensure convergence using Newton's method. If the functions $\{F(\underline{x})\}$ are defined explicitly in terms of $\underline{x}$, then equation 5.4 can be used to compute $[J(\underline{x})]$ exactly.

However, in the formulation proposed by this report, the functions $\{F(\underline{x})\}$ are not given explicitly in terms of $\underline{x}$. Specifically, the equations of motion contain expressions for the creep forces. These creep forces are calculated by using the finite element method. Thus these terms cannot be differentiated analytically.

Instead, the Jacobian matrix is computed numerically. The differential in equation 5.4 is approximated using the trapezoidal rule:

$$\frac{\partial F_i(\underline{x})}{\partial x_j} \cong \frac{F_i(\underline{x} + \underline{\varepsilon}) - F_i(\underline{x})}{\varepsilon} \qquad [5.9]$$

where,

$\varepsilon_k = 0 \qquad k = 1, 2, \ldots, n \qquad k \neq j$

$\varepsilon_j = \varepsilon$

The vector $\underline{\varepsilon}$ has the effect of perturbing the j'th component of the solution vector $\underline{x}$. Thus $F_i(\underline{x})$ is varied with respect to x_j.

If ε is chosen sufficiently small, then equation 5.9 provides a good approximation to equation 5.4. In this analysis, ε was chosen to be a fraction of x_j:

$$\varepsilon = cx_j \qquad [5.10]$$

where $c << 1$. This provided a consistent perturbation of $\underline{x}$ when the components of $\underline{x}$ varied greatly in magnitude.

Several test cases were completed to verify that equation 5.9 was a good approximation for the Jacobian matrix. The tests used a set of polynomial functions that could be differentiated exactly. These tests showed that for $c = 10^{-4}$, excellent agreement was obtained between equations 5.4 and 5.9.

5.3 *Computer Implementation of Newton's Method*

One of the attractive features of Newton's method is that it is easily implemented in a computer program. The computer program CURV written to solve the nonlinear equations of motion is briefly discussed below.

The flowchart for the program is shown in Figure 25. The program begins by reading data for the initial guess of the solution vector, $\underline{x}$, and for the convergence tolerance, δ. Additionally, all other program variables and arrays are initialized.

Next, the iteration loop begins. The function vector $\{F(\underline{x})\}$ is calculated using the equations summarized in Section 3.4. The program must decide to use either the single-point or the two-point contact equations. This is done by considering the maximum lateral displacement that the wheelset can undergo before flanging, x_f. The

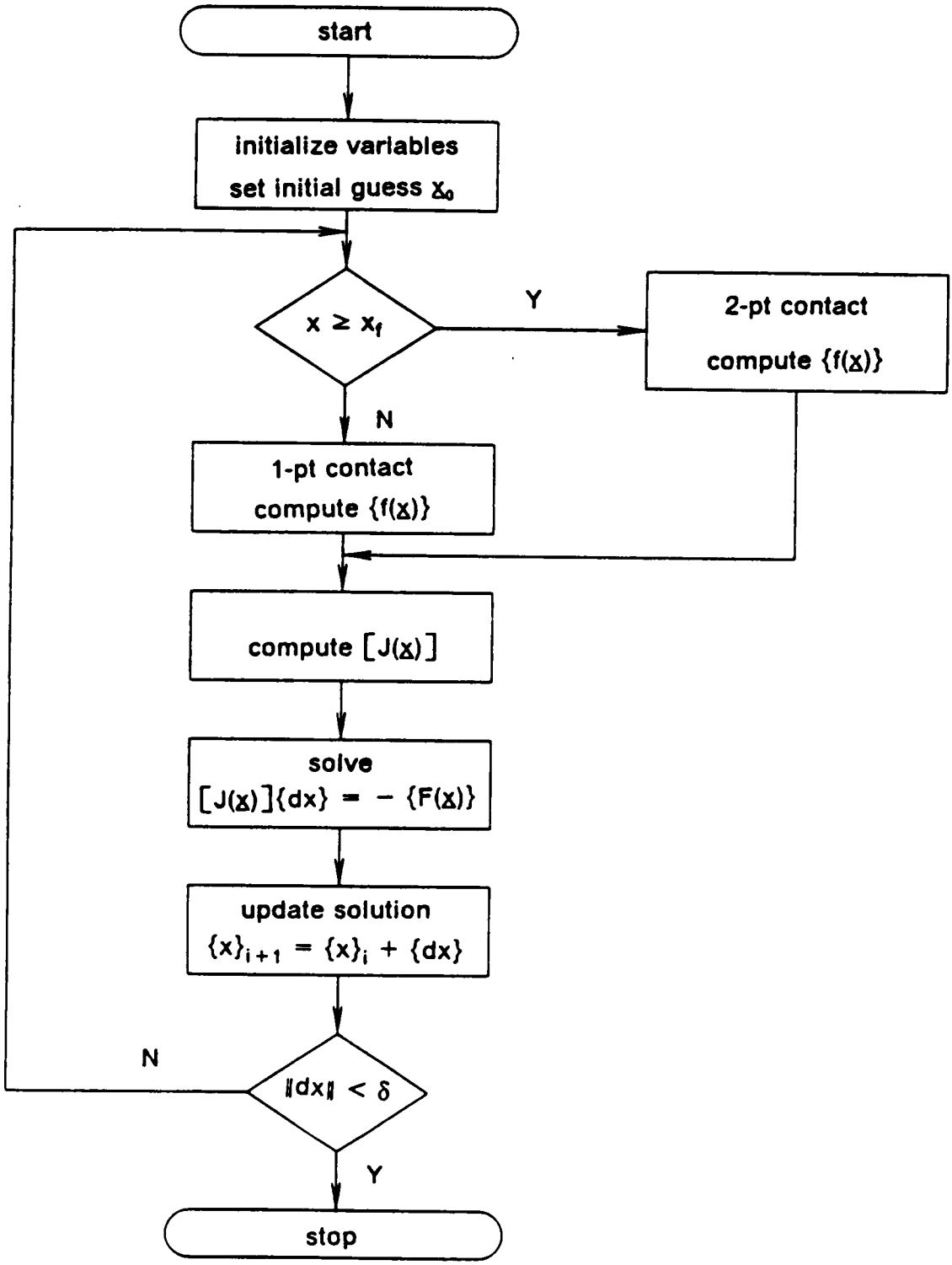

Figure 25. Flowchart for Nonlinear Equation Solver

program checks for flanging by comparing the wheelset lateral displacement, x, to x_f:

$x < x_f$ program uses single-point contact equations

$x \geq x_f$ program uses two-point contact equations

The Jacobian matrix $[J(\underline{x})]$ is computed using equation 5.9.

The system of equations $[J(\underline{x}_i)]\{dx\}_{i+1} = -\{F(\underline{x}_i)\}$ is solved using Gauss elimination. Then the solution vector is updated using $\{x\}_{i+1} = \{x\}_i + \{dx\}_{i+1}$. The norm $\|dx\|_\infty$ is computed and compared to the convergence tolerance. If $\|dx\|_\infty < \delta$, then $\{x\}_{i+1}$ is taken as the solution. Otherwise, the program begins a new iteration.

5.4 Example Problem Using Kalker's Theory

An example problem is presented here to demonstrate the operation of program CURV. In order for CURV to evaluate the function vector $\{F(\underline{x})\}$, it must be able to solve for the creep forces. For this solution, Kalker's linear theory is used to calculate the creep forces. The creep force saturation is computed according to the modified Vermeulen-Johnson model (Nagurka, et al., 1982).

Kalker's linear theory is given by equation 2.12 in Section 2.3. The creep force coefficients $F_{i,j}$ in equation 2.12 are computed by the wheel/rail characterization program WHRAIL (see Section 2.1). The creepages ζ_i are derived by Nagurka (1983). The steady-state creepage expressions are summarized below:

$$\zeta_{LA_{L,R}} = -\, r_{L,R}\rho\theta \sec(\varphi \pm \delta_{L,R}) \qquad [5.11a]$$

$$\zeta_{SP_{L,R}} = -\, \rho \sin(\varphi \pm \delta_{L,R}) - \frac{1}{R}\cos(\varphi \pm \delta_{L,R}) \qquad [5.11b]$$

$$\zeta_{LO_{L,R}} = 1 \pm \frac{a}{R} - r_{L,R}\rho \qquad [5.11c]$$

where ,

$r_{L,R}$ = left and right wheel rolling radii

r_0 = nominal wheel radius

ρ = $\frac{1}{r_0} + \frac{\beta}{V}$.

The creep forces are calculated in subroutine CFORCE of program CURV.

The example problem is illustrated in Figure 26. A wheelset traverses a constant radius curve with velocity V. The track semi-gage length and superelevation are typical for track found in the United States. The wheelset profile used in this example is the CNA 33-inch profile. The rail profile is the AREA 132-lb rail. The various constraint functions for the wheel/rail pair (roll angle, wheel/rail contact position) are shown in Figure 2 of Section 2.1 (page 12). The lateral displacement at flanging, x_f, is determined from the wheel contact position function. The flange contact occurs at the point where the contact position function becomes discontinuous. The value of x_f is the corresponding value for the wheelset lateral displacement. For this problem, x_f = 0.0325 ft.

In the first case run with this example, the curve radius is held constant (R = 1145 ft) and the wheelset velocity is varied. As the velocity changes, the wheelset centrifugal

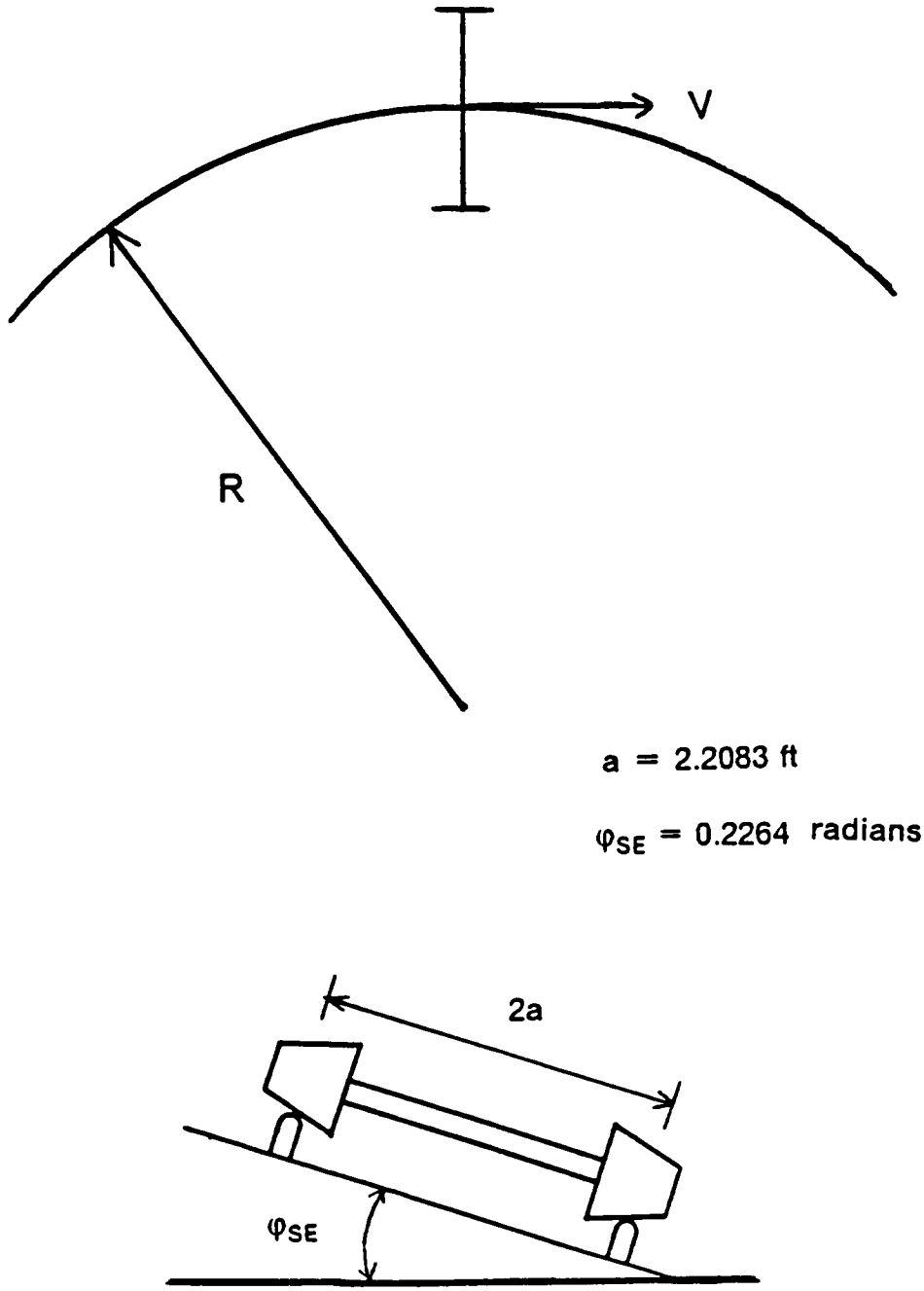

Figure 26. Example Wheelset Curving Problem

force changes as well. This wheelset loading is expressed in terms of the cant deficiency, φ_D :

$$\varphi_D = \frac{V^2}{Rg} - \varphi_{SE} \qquad [5.12]$$

The cant deficiency is a measure of the unbalance between the resultant wheelset body forces and the normal forces. The body forces are the centrifugal and gravity forces. When $\varphi_D = 0$, the body forces are balanced by the normal forces at the wheel. This condition is referred to as balanced running. When $\varphi_D \neq 0$, then there is a net lateral force acting upon the wheelset. This force is represented by the term $mg\varphi_D$ in the steady-state lateral equations (see eq. 3.41 and 3.47). The net lateral force is reacted by creep forces acting at the contact patches.

The results for the wheelset lateral displacement and yaw rotation are shown in Figure 27. The wheelset remains in single-point contact for this case. The yaw angle varies nearly linearly with the cant deficiency. This demonstrates the coupling between the wheelset yaw and lateral load. This coupling is shown in the lateral creepage expression: $\zeta_{LA} \cong -\theta$. The wheelset yaw produces a lateral creepage, and by equation 2.12, a lateral creep force. This lateral force equilibrates the unbalance force from φ_D. The lateral displacement remains nearly constant.

The change in the wheelset spin angular velocity is shown in Figure 28. The change in spin rate varies nearly linearly with the cant deficiency. This change results in a lateral creepage, as shown by equation 5.11a, and thus a lateral creep force. Therefore the change in spin velocity is also coupled to the net lateral load.

The normal loads at the wheels vary nearly linearly with φ_D as shown in Figure 29.

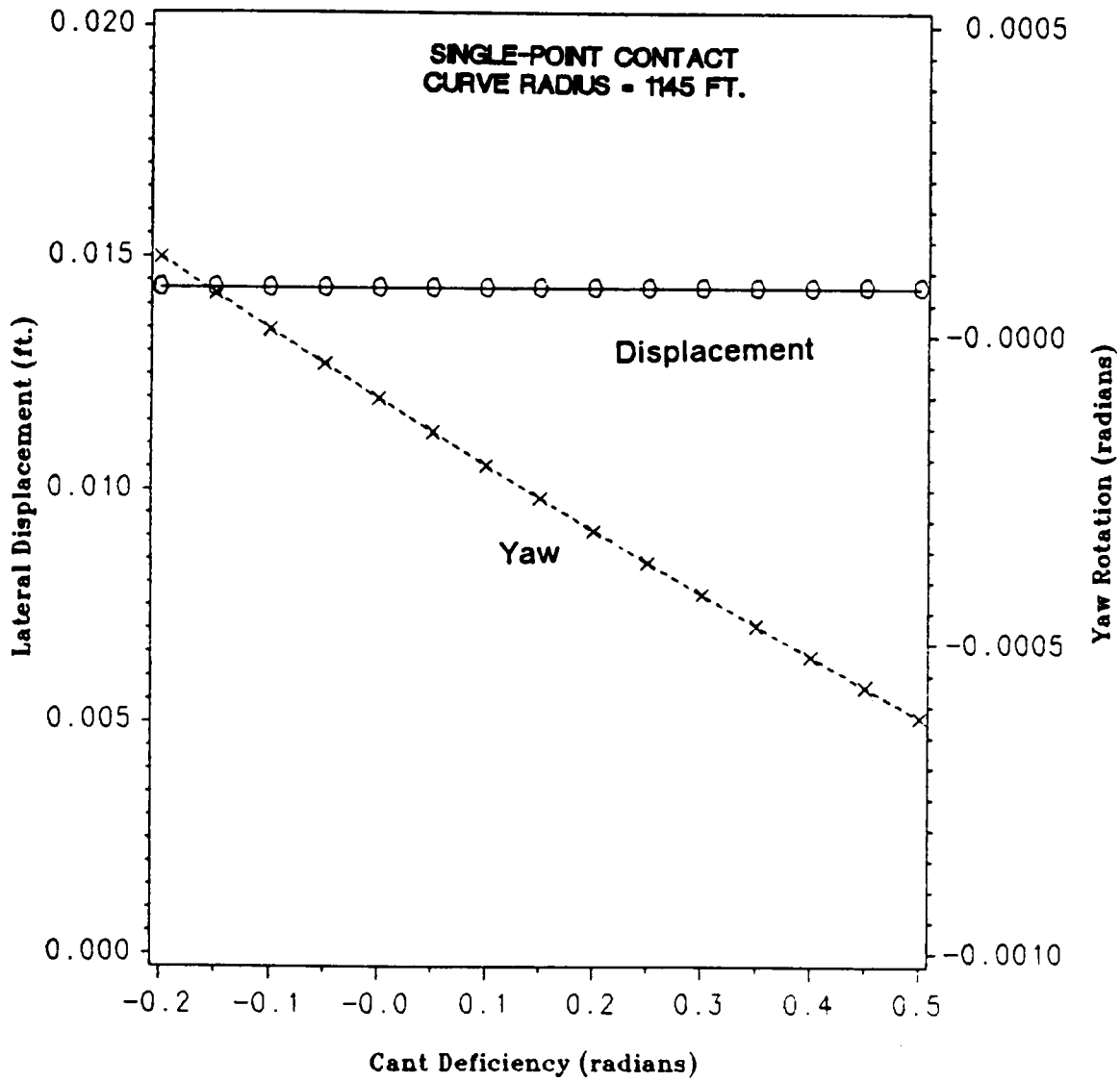

Figure 27. Displacement and Yaw Angle Results for Case of Single-Point Contact

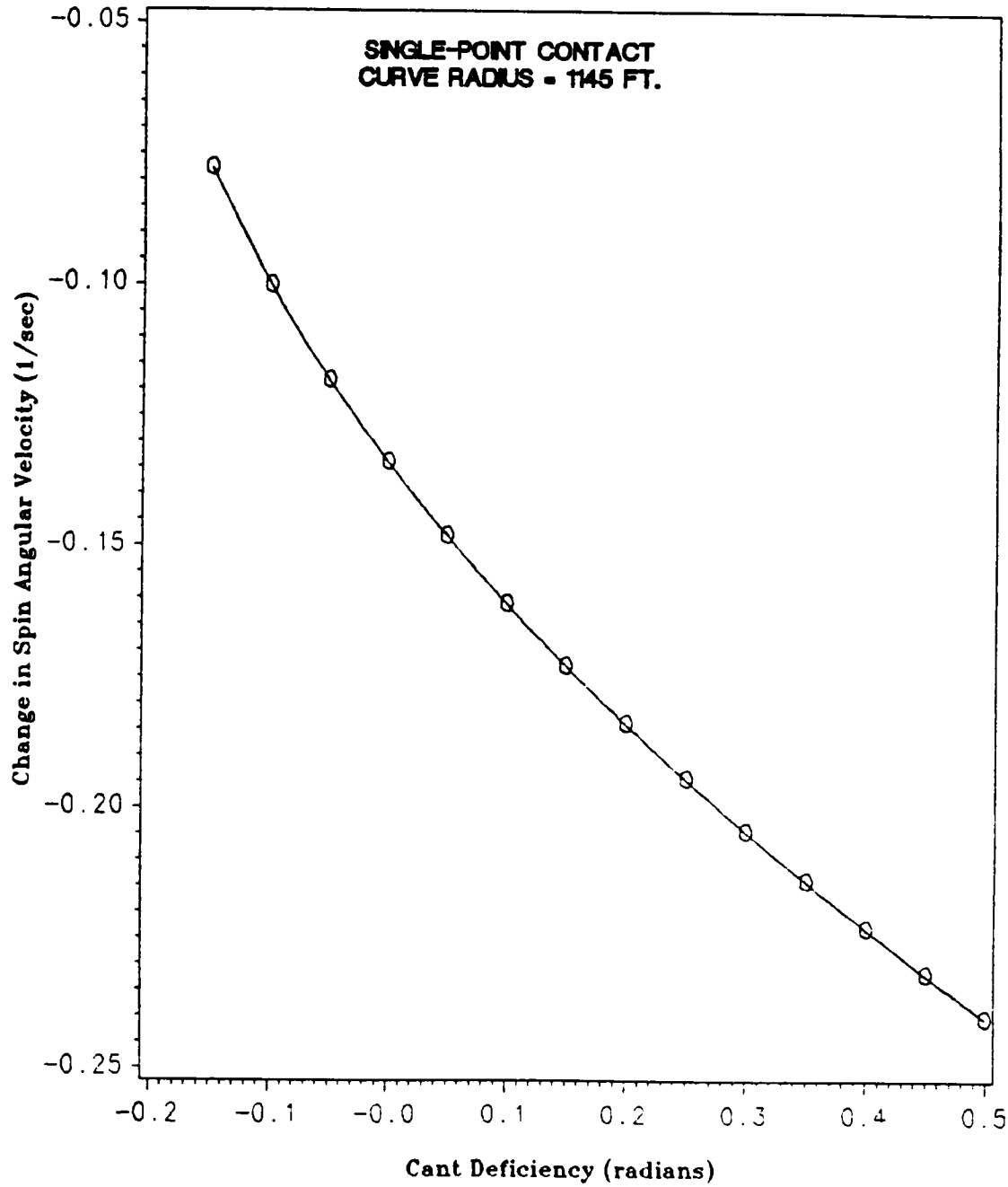

Figure 28. Change in Wheelset Spin Angular Velocity for Case of Single-Point Contact

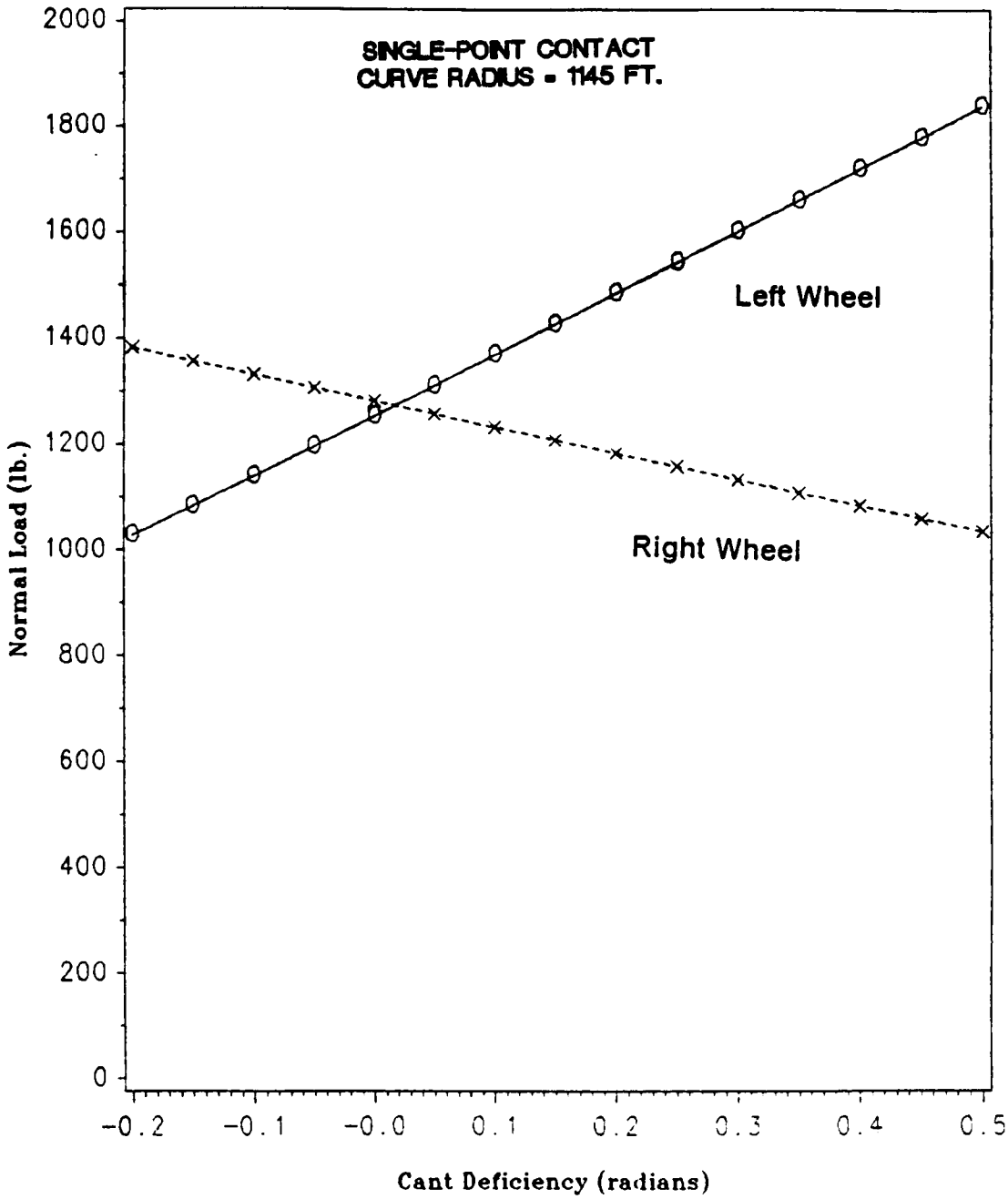

Figure 29. Normal Load Shift for Case of Single-Point Contact

The left and right normal loads are nearly equal for φ_D equal to zero, which is expected for balanced running. The normal load becomes greater at the left wheel for positive φ_D, and becomes greater at the right wheel for negative φ_D.

In the second case, the wheelset velocity is held constant (V = 75 ft/sec) and the curve radius is varied. As the curve radius decreases, a net moment is produced at the wheelset. This net moment is in the yaw direction and is a result of the change in the longitudinal creep forces at the wheels. These forces are proportional to the longitudinal creepages:

$$F_{LO_{L,R}} = -F_{33}\zeta_{LO_{L,R}} = -F_{33}\left(1 \pm \frac{a}{R} - r_{L,R}\rho\right) \qquad [5.13]$$

Thus a decrease in the curve radius R causes F_{LO_L} to decrease and F_{LO_R} to increase. The result is a net moment acting on the wheelset.

The results for the wheelset lateral displacement and yaw rotation are shown in Figure 30. As the curve radius decreases, the wheelset moves laterally until flange contact occurs. This result demonstrates the coupling between the wheelset lateral displacement and the yaw moment. The lateral displacement has the effect of reducing the change in the longitudinal creep forces, and thus the net moment. This is shown by assuming that the rolling radius is proportional to the lateral displacement of the wheelset:

$$r_{L,R} = r_0(1 \pm \Delta x) \qquad [5.14]$$

where Δ is the conicity of the wheel. Substituting equation 5.14 into the longitudinal creep force expression yields:

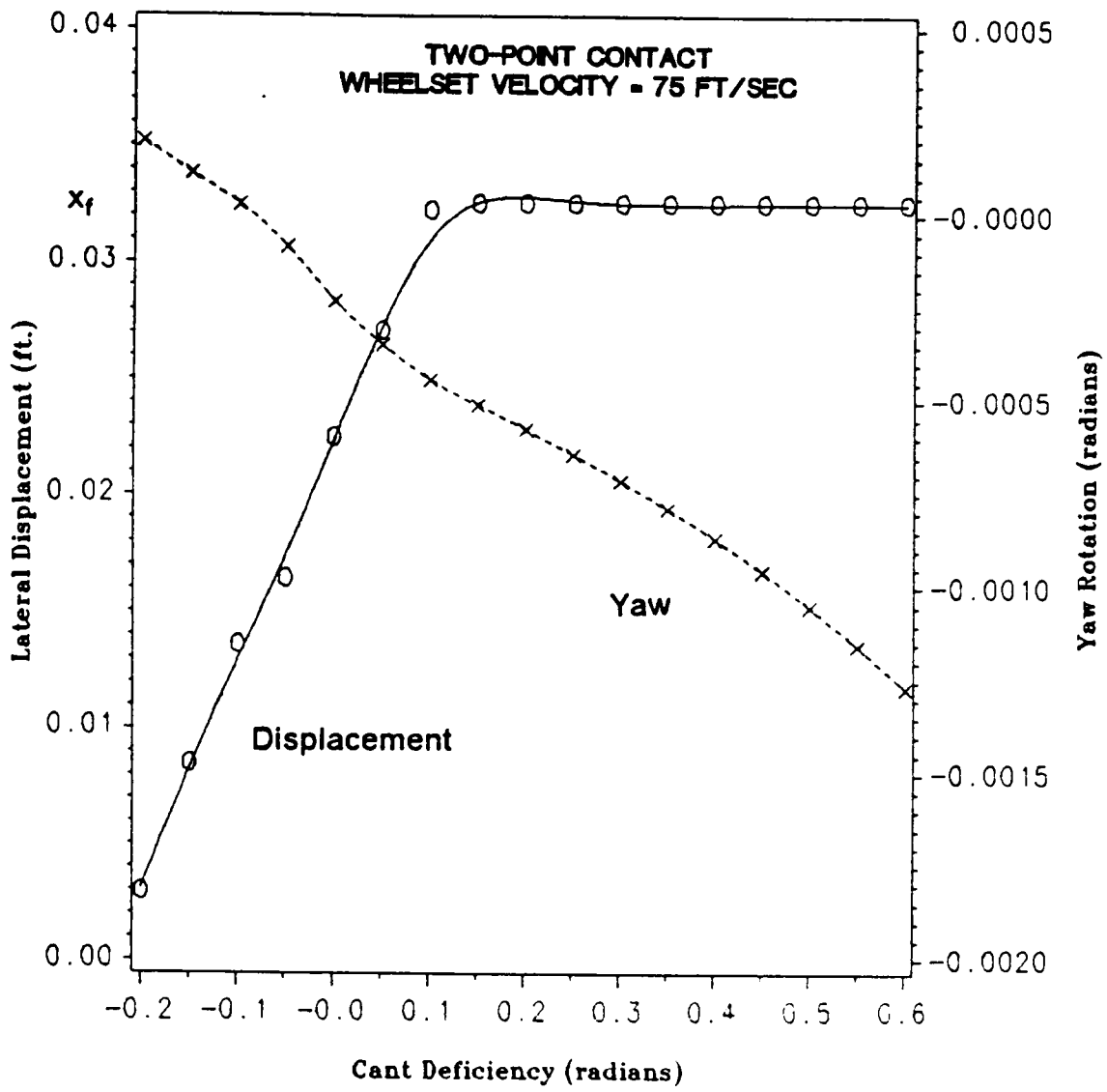

Figure 30. Displacement and Yaw Angle Results for Case of Two-Point Contact

$$F_{LO_{L,R}} \cong -F_{33}\left[\pm \frac{a}{R} \mp \Delta x - \frac{\dot{\beta}}{\Omega} \right] \qquad [5.15]$$

where Ω is the nominal wheelset spin rate, $\Omega = \frac{V}{r_0}$. Thus the net moment produced by the decreasing radius R is balanced by an increase in the lateral displacement x.

When the wheelset flanges, the lateral displacement is constrained. Then the wheelset cannot undergo a lateral displacement to balance any further yaw moment. In this case, the longitudinal creep forces that develop at the flange and tread of the left wheel are in opposite directions. This provides the additional balancing moment to equilibrate the effect of the decreasing radius. In addition, the change in spin angular velocity contributes to reducing the net yaw moment.

The change in spin angular velocity is shown in Figure 31. The spin rate varies nearly linearly with cant deficiency. As in the first example, this change produces a lateral creep force that balances the net lateral body force. Also, as is shown in equation 5.15, the change in spin rate affects the longitudinal creep force. This change contributes to the reduction of the net yaw moment produced by the longitudinal creep force imbalance.

The normal forces at the wheels behave much the same as in the first case, as shown in Figure 32. As φ_D becomes positive, the normal load becomes greater at the left wheel. When flanging occurs, a normal force develops at the flange. This normal force increases as the curve becomes more severe. The normal force on the tread of the left wheel reaches a peak after flange contact. This normal force then decreases as the curve becomes more severe. Eventually the normal force at the tread would reach zero and contact would cease at the tread. Then the wheelset would be

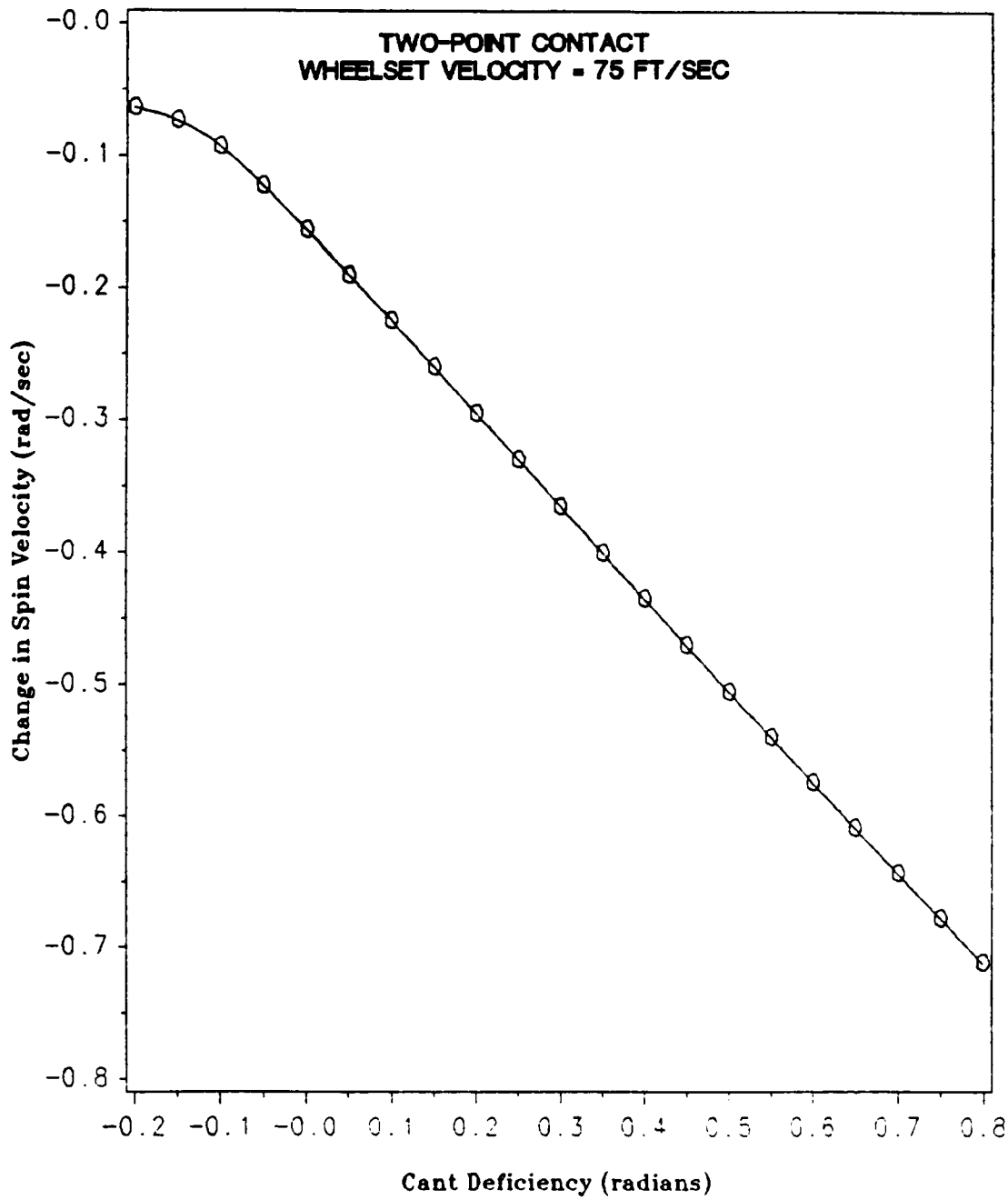

Figure 31. Change in Wheelset Spin Angular Velocity for Case of Two-Point Contact

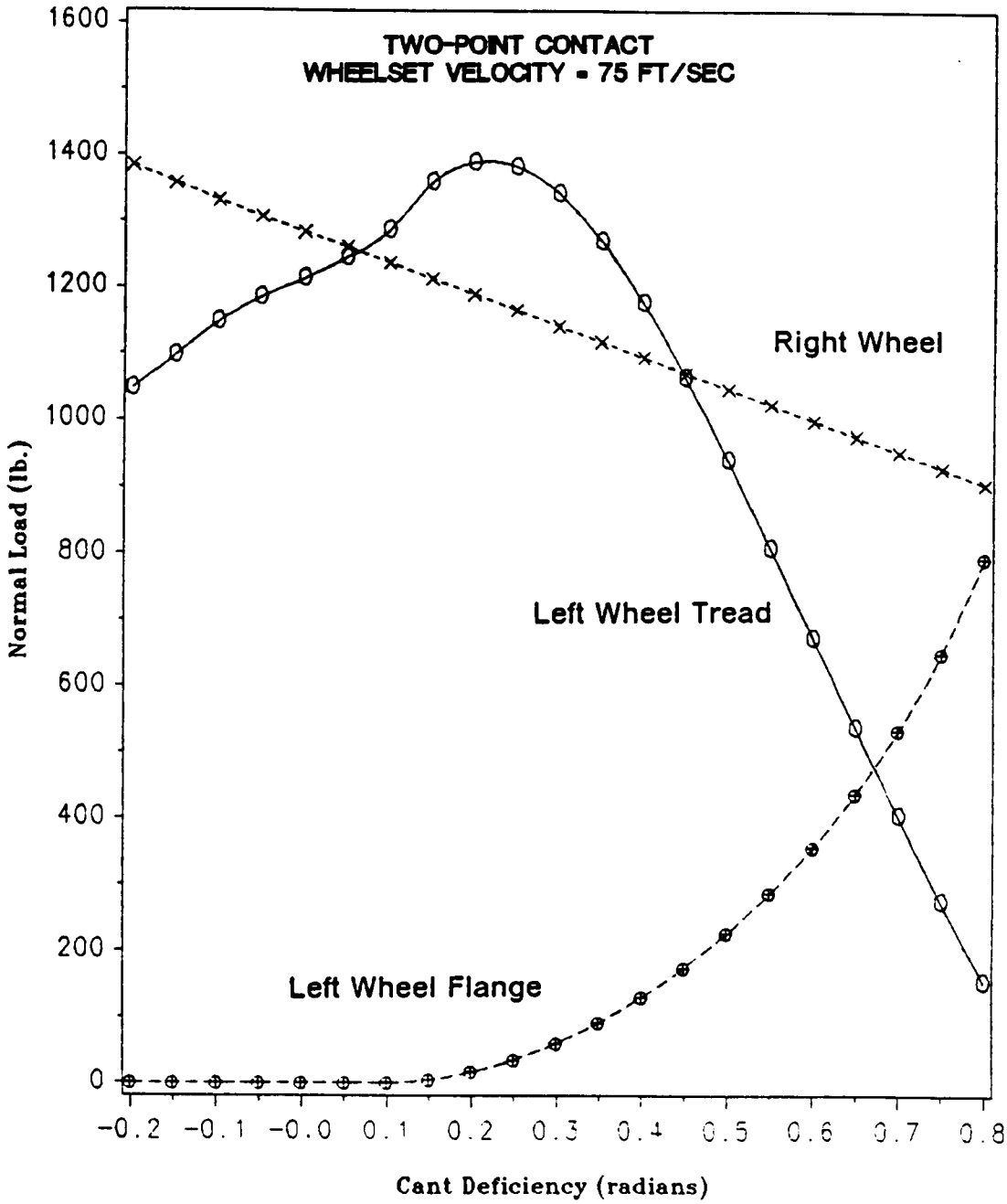

Figure 32. Normal Load Shift for Case of Two-Point Contact

in a condition of single-point contact again; the contact position on the left wheel would be on the flange. This condition is referred to as wheel climb and is a precursor to derailment.

These two cases have demonstrated the important characteristics of a wheelset in steady-state curving. These are summarized below:

- The wheelset yaw is coupled to the wheelset lateral load. A cant deficiency results in a lateral force unbalance and wheelset yaw.

- The wheelset lateral displacement is coupled to the wheelset yaw moment. In curving, a yaw moment is produced from the unbalance of the longitudinal creep forces.

- During flanging, the longitudinal creep forces developed at the two contact points of the flanging wheel are in opposite directions. This produces a moment that balances the net yaw moment due to curving.

- The normal loads at the wheels are proportional to the cant deficiency for single-point contact.

- The change in the wheelset spin angular velocity is proportional to the cant deficiency.

5.5 Summary

Newton's method was used to solve the nonlinear, algebraic, steady-state wheelset equations of motion. The computer implementation of the method was discussed. An example problem was presented that used a heuristic theory to calculate the saturating creep forces. The program results for this example were discussed in detail.

Chapter 6

Summary, Conclusions, and Recommendations

6.1 Summary

The motion of a rail vehicle on a curved track is governed by the creep forces that develop at the wheel/rail interface. Most curving studies use a creep force law that assumes a condition of Hertzian contact geometry at the interface. However, this assumption is invalid for contact near the wheel flange and for worn wheels. The purpose of this work was to investigate the use of the finite element method for predicting the creep forces and solving the steady-state curving problem.

The mechanics of wheel/rail contact were investigated. Several methods for calculating the wheel/rail contact forces were presented. The wheelset equations of motion for the general problem of two-point contact were derived. The generalized forces in these equations were the creep forces and moments. The finite element

program ABAQUS was tried unsuccessfully as a method to solve for the creep forces. Pre- and post-processor programs were written to facilitate the finite element analysis. Several examples of the finite element method solution of static contact problems were presented. These results compared well to theory and other published results. However, the finite element method was not successful in solving the rolling contact problem. The nonlinear steady-state equations of motion were solved using Newton's method. An example steady-state curving problem demonstrated the basic characteristics of a wheelset: the lateral motion is coupled to the net yaw moment, and the yaw rotation is coupled to the net lateral load. The steady-state curving algorithm described by this report is ready to implement the finite element solution of the creep forces.

6.2 *Conclusions*

The finite element method can be used to analyze static contact problems. The method was verified for both Hertzian and non-Hertzian contact examples. Thus this method can be used to determine the contact patch boundary and contact pressure distribution for the wheel/rail interface.

The finite element program ABAQUS was not successful in solving the rolling contact problem. The method correctly predicted saturated creep forces for large creepages. However, the finite element results for small creepages did not match the results of Kalker's theory. It appears that the primary reason is that the contact element could not be made sufficiently stiff in shear. As the element's shear stiffness was in-

creased, the creep forces approached Kalker's theory. However, the solution algorithm failed to converge before the correct creep force value was obtained. Another contributor may be that the mesh was not sufficiently refined. However, the model used in this analysis allocated practically all the storage available to the program.

The finite element method was very costly for solving the contact problem. The computational effort required for the highly nonlinear problem was tremendous. A typical static analysis required approximately 1000 seconds of CPU time on an IBM 3090. A typical rolling contact problem required on the order of 10,000 seconds of CPU time. Even if the method were successful in calculating the creep forces, the cost may be prohibitive for a practical analysis.

6.3 *Recommendations*

Future research should investigate the ability of the finite element method to model rolling contact with slip. The ABAQUS program should be studied further to find ways to improve the convergence of the nonlinear solution algorithm. This may be possible through mesh refinement, or by improved modelling of the rolling contact boundary conditions. As research continues in this field, other programs may become available that can solve the rolling contact problem. These should be studied to find if they offer any improved features compared to ABAQUS.

If this method is not successful, a contact element could be developed with the desired capability. This approach is advantageous in that it allows complete specifica-

tion of the constitutive properties. Such an element could be incorporated into an existing commercial finite element code. Alternatively, the element could be incorporated into a finite element program developed solely for the rolling contact problem. Such a code would be more limited than a general purpose commercial code, but may be more efficient. Thus the solution time may be reduced, making the contact problem more tractable.

References

ABAQUS Theory Manual, 1984, Hilbert, Karlsson, and Sorensen, Inc., Providence, RI.

ABAQUS User's Manual, 1985, Hilbert, Karlsson, and Sorensen, Inc., Providence, RI.

Bathe, K.J., 1982, Finite Element Procedures in Engineering Analysis, Prentice Hall, Inc., Englewood Cliffs, NJ.

Bathe, K.J., and Chaudhary, A., 1985, "A Solution Method for Planar and Axisymmetric Contact Problems,", Int. J. of Numerical Methods in Eng., Vol. 21, pp. 65-88.

Boocock, D., 1969, "Steady-State Motion of Railway Vehicles on Curved Track," J. of Mechanical Eng. Science, Vol. 11, No. 6, pp. 556-566.

Boresi, A.P., Sidebottom, O.M., Seely, F.B., and Smith, J.O., 1978, Advanced Mechanics of Materials, 3rd Ed., John Wiley and Sons, New York, NY.

Cooperrider, N.K., Law, E.H., 1981, "The Nonlinear Dynamics of Rail Vehicles in Curve Entry and Negotiation," 7th IAVSD-IUATAM Symposium on the Dynamics of Vehicles on Roads and Track, Cambridge, U.K. .

Cooperrider, N.K., Law, E.H., Hull, R., Kadala, P.S., and Tuten, J.M., 1975, "Analytical and Experimental Determination of Nonlinear Wheel/Rail Geometric Constraint," FRA-OR&D-76-244, USDOT, December.

Davila, C., 1986, "Prediction of Wheel Wear Profiles by Analytical Methods," Master's Thesis, Department of Mechanical Engineering, VPISU, Blacksburg, VA.

Elkins, J.A., and Gostling, R.J., 1977, "A General Quasi-Static Curving Theory for Railway Vehicles," Proceedings 5th VSD-2nd IUTAM Symposium, Vienna.

Elkins, J.A., and Eickhoff, B.M., 1979, "Advances in Nonlinear Wheel/Rail Force Prediction Methods and Their Validation," ASME Winter Annual Meeting, New York, December.

Johnson, L.W., and Riess, R.D., 1982, Numerical Analysis, 2nd Ed., Addison-Wesley Publishing Co., Reading, MA.

Heumann, H., 1931, "Kurzes Lehrbuch des Dampflokomotivebaues," Springer, Berlin.

HKS, 1987, Phone conversation with consulting staff at Hilbert, Karlsson, and Sorenson.

Kalker, J.J., 1967, "On the Rolling Contact of Two Elastic Bodies in Dry Friction," Doctoral Dissertation, Technische Hogeschool, Delft, The Netherlands.

Kalker, J.J., 1979, "Survey of Wheel-Rail Rolling Contact Theory," Vehicle System Dynamics, Vol. 5, pp. 317-358.

Kalker, J.J., 1982, "A Fast Algorithm for the Simplified Theory of Rolling Contact," Vehicle System Dynamics, Vol. 11, pp. 1-13.

Law, E.H., Frank, H., Haque, I., 1986, "Nonlinear Steady-State Curving of Locomotives Equipped with Three Axle Trucks," ASME Winter Annual Meeting, Anaheim, California, December.

Marcotte, P.P., Mathewson, K.J.R., and Young, R., 1981, "A Practical Model of Rail Vehicle Curve Negotiation," 7th IAVSD Symposium, Cambridge, U.K. .

Meirovitch, L., 1970, Methods of Analytical Dynamics, McGraw Hill Book Co., New York, NY.

Nagurka, M.L., 1983, "Curving Performance of Rail Passenger Vehicles," Doctoral Dissertation, Department of Mechanical Engineering, MIT, Cambridge, MA.

Nagurka, M.L., Bell, C.E., Hedrick, J.K., and Wormley, D.N., 1982, "Computational Methods for Rail Vehicle Steady-State Curving Analysis," ASME Winter Annual Meeting, Phoenix, Arizona, November.

Nagurka, M.L., Wormley, D.N., Hedrick, J.K., 1984, "Dynamic Curving Performance of Rail Transit Vehicles," ASME Paper No. 84-WA/DSC-12.

Newland, D.E., 1969, "Steering a Flexible Railway Truck on Curved Track," J. of Eng. for Industry, Vol. 91, No. 3, pp. 908-918.

Paul, B., and Singh, S., 1982, "User's Manual for Program CONWHEEL," Technical Report No. 10, prepared for the FRA/DOT.

Porter, S.R.M., 1935, "The Mechanics of a Locomotive on a Curved Track," The Railway Gazette.

Reddy, J.N., 1984, An Introduction to the Finite Element Method, McGraw Hill Book Co., New York, NY.

Shen, Z.Y., Hedrick, J.K., Elkins, J.A., 1985, "A Comparison of Alternate Creep Force Models for Rail Vehicle Dynamics," Proceedings 8th IAVSD Symposium, Cambridge, MA, pp. 591-605.

Simons, J.W., and Bergan, P.G., 1986, "A Finite Element Formulation of Three-Dimensional Contact Problems With Slip and Friction," Computational Mechanics, Vol. 1, pp. 153-164.

Vermeulen, P.J., and Johnson, K.L., 1964, "Contact of Nonsphrical Elastic Bodies Transmitting Tangential Forces," J. of Applied Mechanics, Vol. 86, pp. 338-340.

The vita has been removed from the scanned document